GEOPHYSICS, VOL. 37, NO. 1 (FEBRUARY 1972), P. 98–141, 36 FIGS.

THE MAGNETOTELLURIC METHOD IN THE EXPLORATION OF SEDIMENTARY BASINS†

KEEVA VOZOFF*

The paper describes the theory of the magnetotelluric (MT) method, and some of the experimental, analytical, and interpretive techniques developed for its use in petroleum exploration in the past five years. Particular emphasis is placed on interpretation, since it is the area least amenable to routine treatment. Whereas present interpretation techniques are adequate, interpretation is the area of both the greatest progress and the greatest need for improvement.

Field results are presented from traverses in South Texas bordering on the Gulf of Mexico, and the Anadarko Basin of southwestern Oklahoma. Wide station spacings were used, such as might typify basin evaluations. The South Texas results are compared directly with smoothed induction logs. No useable logs could be found for Oklahoma. Comparisons with known and inferred geology show that the surveys mapped resistivity successfully in the known parts of these basins as well as in portions inaccessible seismically.

The capabilities and economics of the MT method justify its consideration for evaluating large unexplored blocks and "no record" areas.

NOTATION

x, y, z	Coordinate axes. Positive north, east, and down.
j	Current density, amperes/square meter
V	Potential difference, volts
I	Current, amperes
R	Resistance, ohms
f	Frequency, hertz (hz)
ω	Angular frequency $=2\pi f$, radians/second
ρ	Resistivity, ohm-meters (ohm-m)
σ	Conductivity, mho/m
μ	Permeability, henry/meter (h/m)
μ_0	Free space permeability, $=4\pi\times10^{-7}$ h/m
E	Electric field, volts/meter (practical units—mv/km)
H	Magnetic field, amperes/meter [practical units—gammas (γ)]
E_x	Component of E in the x direction
l	Electrode separation, meters
δ	Skin depth, meters
ρ_a	Apparent resistivity, ohm-m
Z_{ij}	Impedance tensor element relating E_i to H_j, ohms
$Z_i'_j$	Z_{ij} after rotation through θ (in principal axes)
ρ_{ij}	Apparent resistivity corresponding to Z_{ij}
θ_0	Direction of E for largest apparent resistivity, clockwise from north
x', y', z	Coordinate system after rotation through θ (principal axes)
$E_{\|}, H_{\|}$	Components parallel to strike
ϕ	Tipper azimuth measured clockwise from north
S	Skewness
T	Tipper

INTRODUCTION

Advances in magnetotelluric techniques and preliminary indications of success in their use

† Dr. Vozoff's paper is the second in a series of survey papers sponsored by the Research Committee of the SEG. The series was the subject of an editorial in the December, 1971 issue of GEOPHYSICS (v. 36, p. 1252).

Presented at the 39th Annual International SEG Meeting, September 17, 1969, Calgary, Alberta. Manuscript received by the Editor April 30, 1971; revised manuscript received July 20, 1971.

* Professor of Geophysics, School of Earth Sciences, Macquarie University, North Ryde, N.S.W. 2113, Australia.

have led to an acceleration in interest and application. As a rough estimate, more than a million dollars was spent on magnetotelluric (MT) contract fieldwork and research in 1969. For the first time, fieldwork is being supported by the operating divisions of major oil companies as well as by their research laboratories.

This paper is intended to help fill the increasing need of the petroleum geophysicist to understand the method so he can use it intelligently. Field results are included to illustrate the method's potential and its inherent limitations.

BASIC CONCEPTS

The MT method is a way of determining the electrical conductivity distribution of the subsurface from measurements of natural transient electric and magnetic fields on the surface.

Results interpreted from measurements at a single site are sometimes compared to an induction log, very heavily smoothed, obtained without drilling a well. Results from a line of measuring stations are interpreted to give underlying conductivity distribution and structure. That picture of the subsurface can in turn be related to porosity and salinity, since conductivity depends primarily on those two factors in common sedimentary rocks.

The time variations of the earth's electric and magnetic fields at a site are recorded simultaneously over a wide range of frequencies, usually on digital tape. The variations are analyzed by computer to obtain their spectra and apparent resistivities as a function of frequency are computed from the spectra. Interpretation consists of matching the computed plots of apparent resistivity against frequency to curves calculated for simplified models.

The MT method depends on the penetration of electromagnetic energy into the earth. Depth control comes as a natural consequence of the greater penetration of the lower frequencies. The measurements are absolute. Their interpretation gives true resistivity values and true depths, not just anomalies. Depth interpretation based on MT data is therefore much more definitive than that based on gravity or magnetic data.

THE SIGNALS

The time-varying magnetic (H) signal is the always present "noise" in the earth's magnetic field. When very large, it interferes with magnetic surveys. In the conducting earth, the changing magnetic field induces telluric (eddy) currents and voltages: the latter are the electric (E) signals. They are very similar in appearance to the H signals. On chart records, both sets of variations look irregular and noise-like for the most part, as in Figure 1. At times, in certain frequency bands, the variations may appear sinusoidal (Figure 2) but the sinusoids are not an important part of the signal for MT purposes. Signal amplitudes fall off rapidly with increasing frequency over most of the range of frequencies used. Figure 3 shows typical spectral behavior for E and H as recorded in four overlapping frequency bands. Signal level can increase very rapidly at the onset of magnetic storms, an increase of a factor of 10 being common and even a factor of 100 is not unusual.

Most of the magnetic noise reaching the earth below 1 hz is due to current flow in the ionized layers surrounding the earth. The currents are powered by solar activity, and by the relative motions of the earth, sun, and moon. At frequencies above 1 hz, worldwide electrical thunderstorm activity within the atmosphere is the major contributor. The transient fields due to thunderstorms can be exceedingly large locally, while those associated with tornados are greater still.

EFFECT OF EARTH CONDUCTIVITY ON H

When the magnetic fluctuations reach the surface of the earth, reflection and refraction occur. Although there was considerable disagreement at one time, it is now well established that, as a working theory, the signals can be treated as plane electromagnetic waves. This will not be true under all conditions, but holds for the vast majority of geological situations of interest in petroleum prospecting (Madden and Nelson, 1964; Rikitake, 1966; Vozoff and Ellis, 1966).

Although the majority of the incident energy is reflected, a small portion is transmitted into the earth and slowly travels vertically downward. To the conducting rocks, this energy appears as a magnetic field which is changing with time, and electric fields are induced so that currents, called telluric currents, can flow. These telluric currents are completely analogous to the eddy currents which flow in transformers due to the changing magnetic fields caused by the ac current in the primary windings.

Energy in the downgoing disturbance is quickly dissipated as heat. As a result, the field penetration is relatively small in terms of its wavelength in air. The penetration mechanism in this situation is actually diffusion rather than wave propagation.

Current density in the earth depends on resistivity ρ, as might be expected. Within a rock, the normal relationship between the electric field and the current density at each point is

$$j = E/\rho.$$

This differential form of Ohm's law is really a definition of *resistivity*, and is very similar to the Ohm's law definition of resistance,

$$I = V/R.$$

In mks units, E is in volts/meter; j is in amperes/square meter; ρ is in ohm-meters; and H is in amperes/meter. However, because the fields are so small, the more commonly used practical units are mv/km for E and gammas for H. The practical units will be used in later sections.

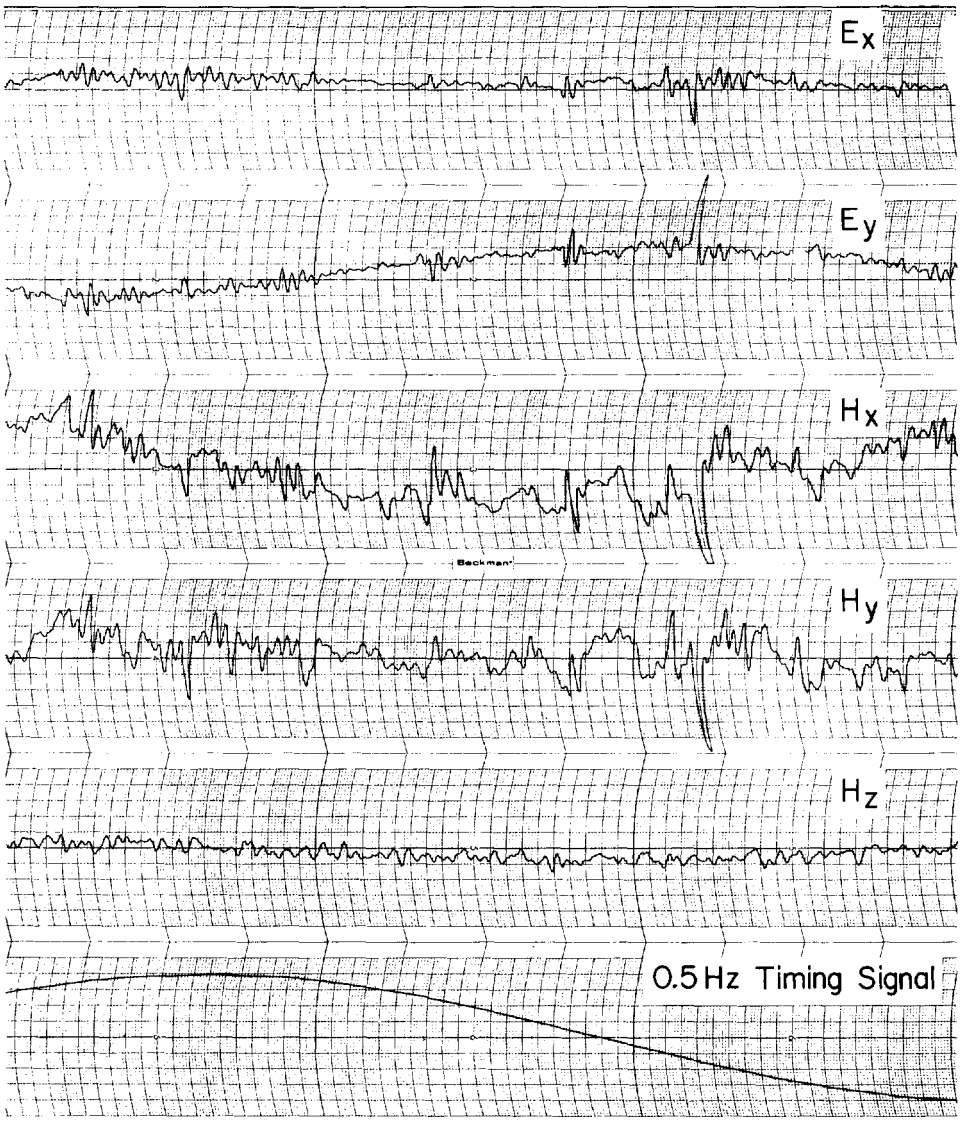

FIG. 1. Typical noise-like telluric signals. Sine wave at bottom shows time scale.

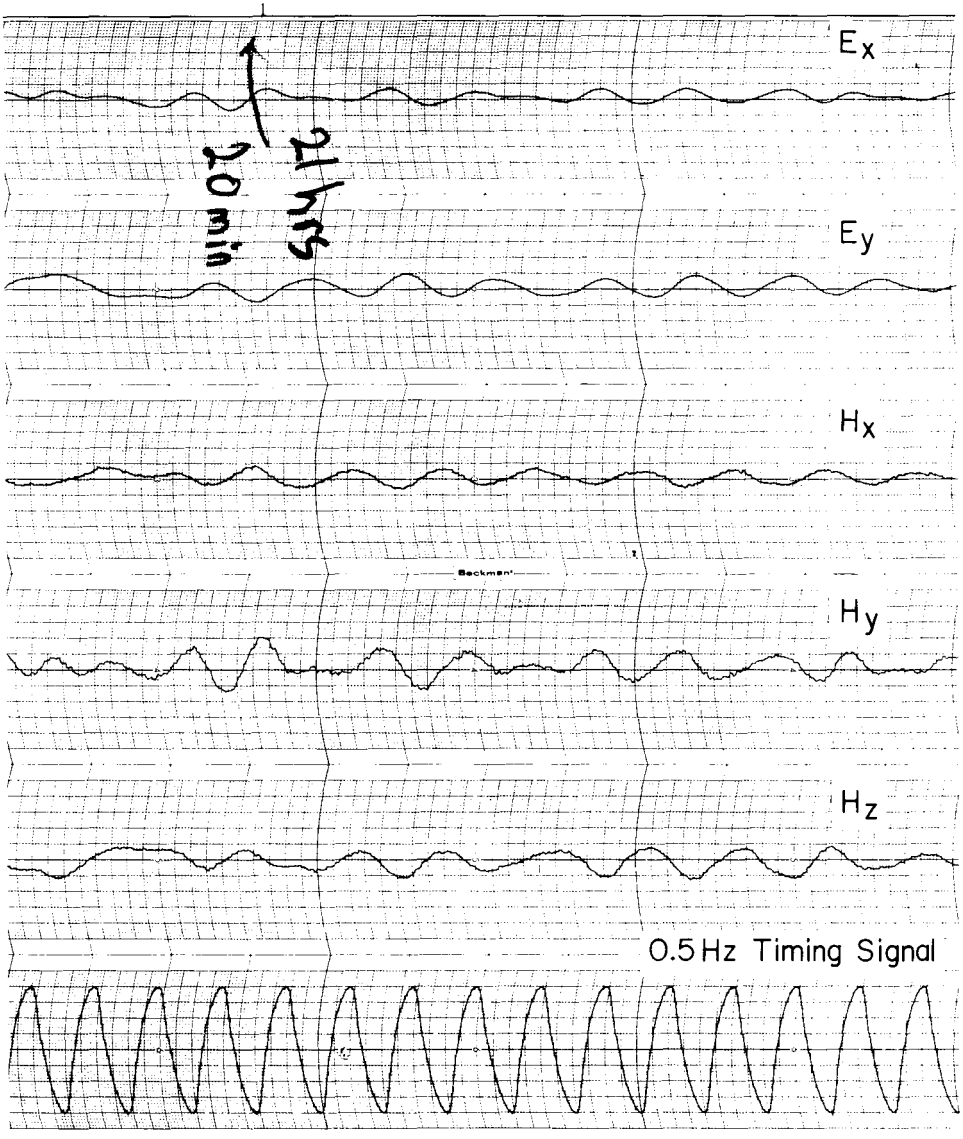

FIG. 2. Large near-sinusoidal telluric signals with superposed noise-like signals. Time scale on bottom trace.

The E measurement is actually a voltage difference measurement between two electrodes. In a uniform earth, the voltage difference V between electrodes a distance l apart would be

$$V = lE.$$

In the MT method it is usually assumed that E is constant over the length of the wire; i.e.,

$$E = V/l.$$

The depth of penetration of the fields into the earth is inversely related to rock conductivity. In a uniform earth E and H weaken exponentially with depth; the more conductive the earth, the less the penetration. The depth at which the fields have fallen off to $(e)^{-1}$ of their values at the surface is called the skin depth δ.

$$\delta = \sqrt{2/\omega\mu\sigma} \text{ m} \tag{1}$$

$$\approx \tfrac{1}{2}\sqrt{\rho/f} \text{ km}, \tag{1a}$$

where f is frequency, $\omega = 2\pi f$, and μ is permeability. (μ in the earth is taken equal to μ_0 except in highly magnetic materials.) Frequency enters into the equations because the magnitudes of the induced telluric currents depend on the time rate of change of the magnetic fields.

In a uniform or horizontally layered earth all currents, electric fields, and magnetic fields are practically horizontal, regardless of the direction from which these fields enter the earth. This comes about because of the high conductivity of earth relative to air. It can be thought of in terms of Snell's law in optics, with the velocity in the earth being orders of magnitude smaller than that outside. Furthermore, the currents and electric fields are at right angles to the associated magnetic fields at each point. If E is positive to the north, H is positive to the east. That is, viewed from above, E must be rotated 90 degrees clockwise to obtain the direction of positive H.

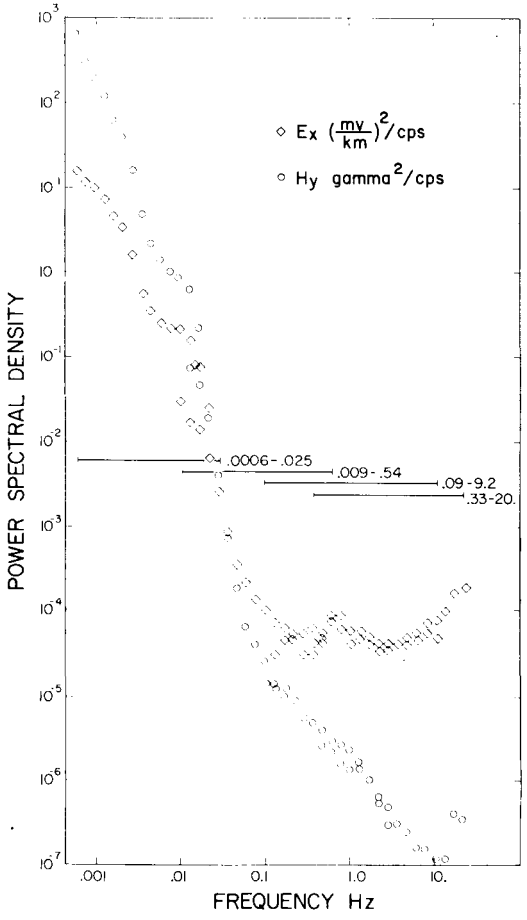

FIG. 3. Selected power spectral densities recorded in the four overlapping frequency bands indicated. Bands were recorded at different times.

The mathematical description of the perpendicular E and H fields in a uniform isotropic conductor includes all these features in a concise form:

$$H_y = H_y^0 e^{-i\omega t-(i-1)z/\delta}; \tag{2}$$

$$E_x = E_x^0 e^{-i\omega t-(i-1)z/\delta}; \tag{3}$$

$$E_x^0 = (1 - i)\omega\mu\delta H_y^0/2. \tag{4}$$

The superscript indicates the value at the surface. Particularly interesting is the ratio

$$\frac{E_x^0}{H_y^0} = \frac{(1 - i)\omega\mu\delta}{2} \text{ ohms} = (1 - i)(\omega\mu/2\sigma)^{1/2}. \tag{5}$$

Since E and H are recorded at frequencies which can be accurately measured and since μ varies little from μ_0 in most rocks, the ratio shows the relationship which exists between the conductivity and the measured fields. The equation can be solved for conductivity, giving

$$\sigma^{1/2} = (1 - i)(\omega\mu/2)^{1/2}\frac{H_y^0}{E_x^0}. \tag{6}$$

Equation (6) is usually rewritten in mks units as

$$\rho = \frac{i}{\omega\mu}\left(\frac{E_x}{H_y}\right)^2 \tag{6a}$$

and the superscripts are omitted.

In practical units, where E is given in mv/km and H is in gammas, the magnitude of ρ is

$$\rho = \frac{1}{5f}\left(\frac{|E_x|}{|H_y|}\right)^2. \tag{6b}$$

When ρ (or σ) is calculated from E and H values, it is called an *apparent* resistivity ρ_a (or apparent conductivity σ_a). ρ and ρ_a are related, but they must be clearly distinguished. ρ_a is the resistivity that a uniform earth must have to give the measured value of the impedance Z. ρ is a property of the medium, whereas ρ_a depends on how it is measured. The ratio of E_i to H_j at each frequency is the impedance Z_{ij} for those components at

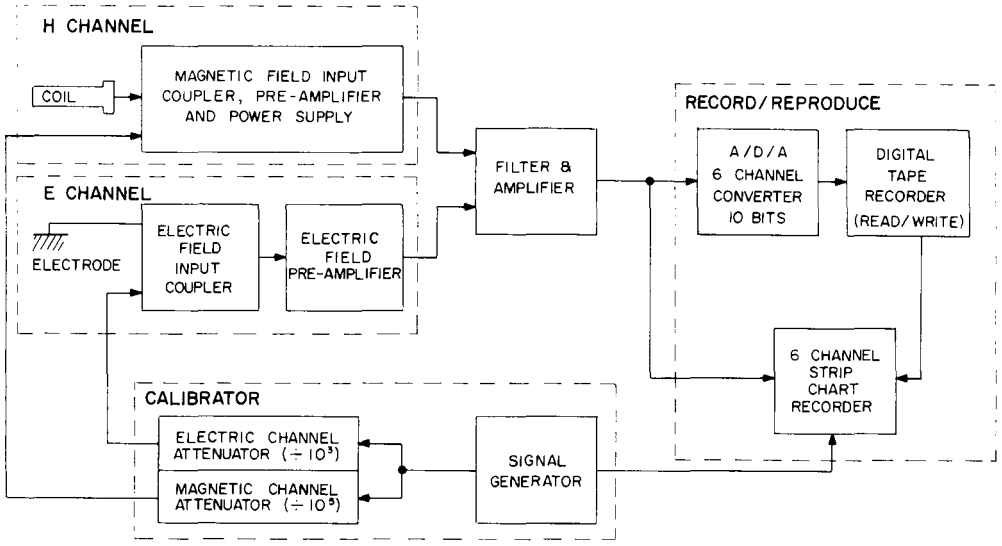

FIG. 4. Block diagram of a basic magnetotelluric instrumentation system.

that frequency. Since E and H are usually not in-phase, Z_{ij} is taken to be a complex number.

In a uniform earth, ρ_a has to be the same at every frequency, and E leads H in-phase by 45 degrees at all frequencies. [That this is so can be checked by substituting equation (5) into equation (6b)]. Thus, if we plot ρ_a and phase against frequency, we see that both are constants.

In discussing kinds of electrical structure it is useful to define two-dimensional and three-dimensional structures. In the two-dimensional case [$\sigma=\sigma(x, z)$], conductivity varies along one horizontal coordinate and with depth. The other horizontal direction is called the strike. When conductivity varies with both horizontal coordinates and with depth [$\sigma=\sigma(x, y, z)$], the structure is said to be three-dimensional and has no strike. If σ depends only on z, the structure is one-dimensional. In each case, σ at each point can depend on the direction of current flow; if σ does depend on direction, the medium is anisotropic.

If the conductivity changes with depth, ρ_a varies with frequency, since lower frequencies penetrate more deeply. Apparent resistivity can be written and computed *exactly* for any desired combination of horizontal layers, whether isotropic or arbitrarily anisotropic. It can be calculated *approximately* for any two-dimensional model structure. As might be expected, Z for horizontally isotropic and homogeneous layers does not depend on the directions used as long as E is measured perpendicular to H.

When due to faulting or jointing, σ varies laterally or with direction, the j and E which are induced by a given H depend on their direction relative to strike. In order that these effects can be sorted out, we record complete horizontal E and H fields (two perpendicular components of each) at every site. In addition, the vertical component of H is also recorded, for a total of five recorded signals in all. These are designated H_x, H_y, H_z, E_x, and E_y.

In general, ρ_a at each frequency varies with measurement direction. We assume that there is a strike but that its direction is unknown. Then E_x is due partly to H_y, but also partly to currents induced by H_x, which have been deflected by the structure. The same is true of E_y, so the relations are written

$$E_x = Z_{xx}H_x + Z_{xy}H_y, \tag{7}$$

$$E_y = Z_{yx}H_x + Z_{yy}H_y. \tag{8}$$

For example, Z_{yx} gives the part of E_y which is due to H_x, and so forth. Since E_y and H_x are generally not in-phase, the Z's are complex. E and H component amplitudes are obtained by computer-analyzing the records using methods described in the section on data analysis. Computation of the Z_{ij} for two-dimensional models will be discussed under Interpretation.

INSTRUMENTATION

Over most of the frequency range of 0.0006–10 hz used for most MT work, the signals weaken rapidly with increasing frequency. Figure 3 shows typical (smoothed) power density spectra in this range. The absolute levels can rapidly increase by 30 db or more on the advent of a magnetic storm. They are also often observed to gradually diminish by 10–20 db in a matter of hours. Furthermore the detailed shape of the spectrum changes, with some frequency bands being enhanced relative to the general trend. Heirtzler and Davidson (1967) show a sample of these variations in H, for the component along the main geomagnetic field.

A block diagram of a typical measuring system is shown in Figure 4. The complete equipment set includes three H channels and two E channels. Of the components, nearly all are custom-made except for the signal generator, E field preamplifiers, strip chart recorder, and the digital recording system. A single 1 kva liquid propane-powered motor generator will operate the system.

The H sensors are long, slender induction coils comprised of 30,000 turns of #22 copper wire wound on cores laminated of moly-permalloy strips. The strips are 1 inch wide and 6 ft long, filling a $1\frac{1}{3}$ inch diameter tube. Earth contacts for E sensors are nonpolarizing electrodes made up of cadmium metal immersed in a cadmium chloride solution, in porous pots $1\frac{3}{4}$ inches in diameter and $2\frac{3}{4}$ inches high. (The solution is highly toxic!)

The other highly critical component is the H preamplifier. This is a guarded, differential input, chopper carrier amplifier with very low-noise connections and components, with heat sinks and shock mounts. No common commercial amplifiers have yet been found which can be fed by the high inductance coils while retaining the bandwidth, low noise, and high gain necessary in this application.

The rest of the system was designed for geophysical field use. Its response is accurately known, but its specifications are not otherwise remarkable.

Rather than record the entire frequency range at once, the 10^{-3} to 10 hz band is recorded in

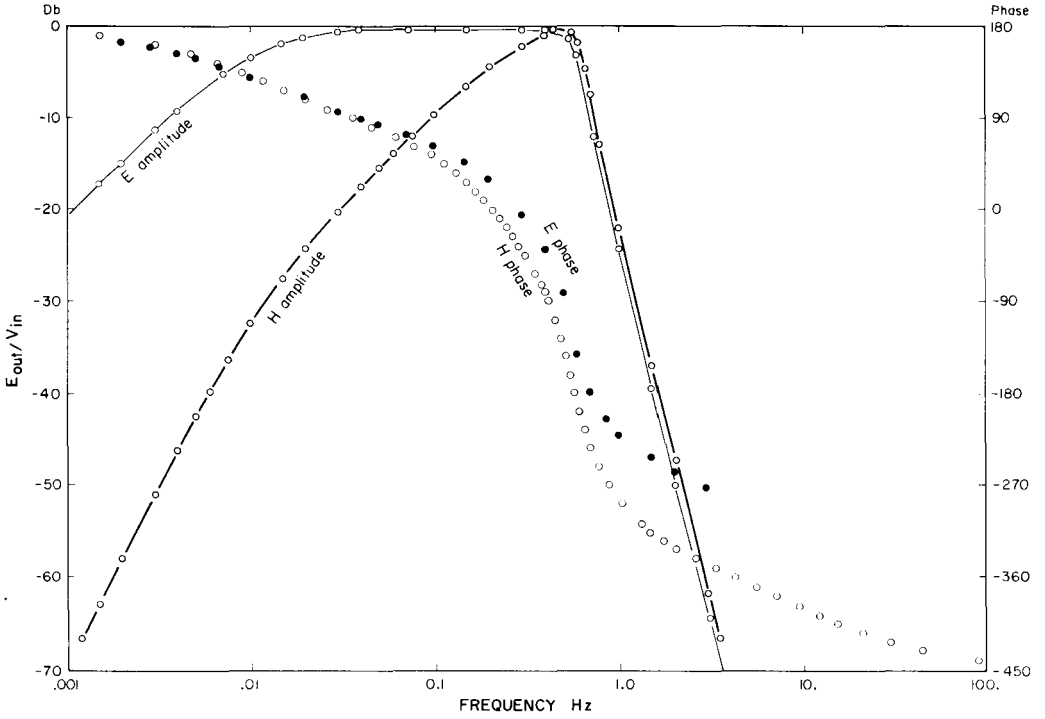

FIG. 5. Responses of commercial E and H systems in one typical recording band.

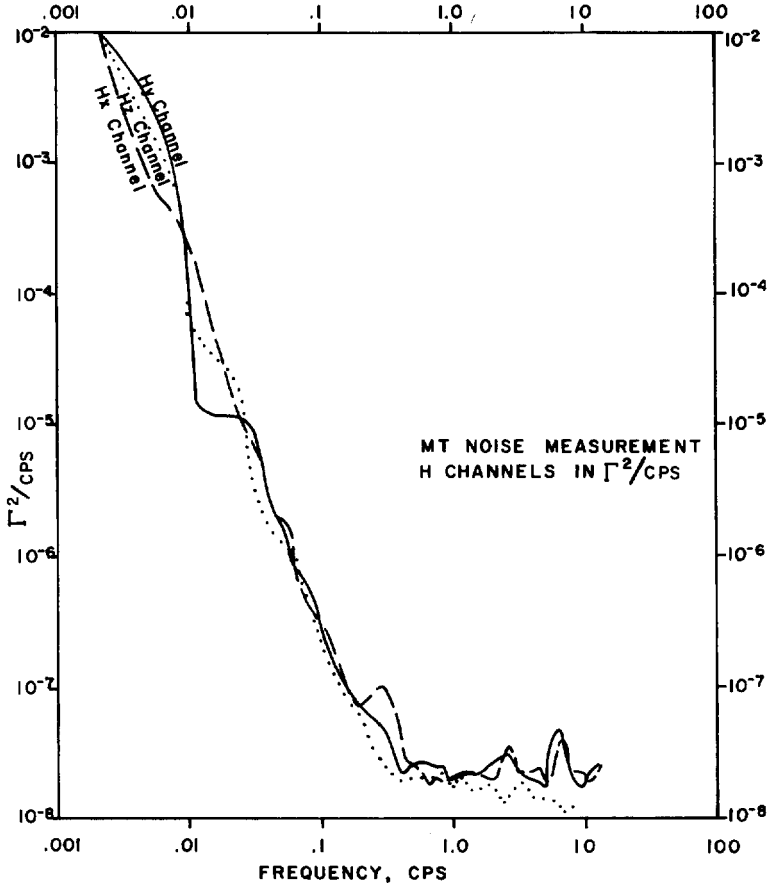

FIG. 6. Noise power spectral density of commercial H system. Obtained using noise measurement procedures of Hopkins (1965).

three narrower, overlapping segments. Commonly these are (nominal) 0.002–0.025, 0.01–0.5, and 0.1–7.5 hz, with $\Delta t = 10$ sec, 0.5 sec, and 1/30 sec, respectively. (Δt is the sampling rate of the digital equipment.) Other filter settings can be used when desired. The actual frequency range analyzed extends from 0.0006 to 9.8 hz. In areas of high near-surface resistivity, a still higher frequency band is recorded, extending from 0.33 to 15.5 hz ($\Delta t = 1/37.5$ sec). The frequency range is divided this way for two important reasons: to make best use of the available dynamic range and for economy in digital recording. That is, dividing the frequency range permits the use of large gains in some parts of the spectrum and lower gains in others, according to the signal levels actually present at recording time. The economic aspect enters, since the total recording duration is a multiple of the longest period which is being recorded, whereas digitizing rate is at least twice the highest frequency being recorded. If the band is very wide, far more short period data will be acquired than is necessary while waiting for adequate sampling of long periods. The 1- to 2-decade segments used are a compromise.

Total number of samples to be recorded in a data set is selected in this equipment by means of a front panel switch. Most commonly, data sets consist of 4096 multiplexed scans. Each voltage sample is converted to a 10 bit binary number, giving a full scale resolution of 2^{-10} or about 60 db.

Typical normalized system response curves are shown in Figure 5. In terms of the parameters measured, the maximum full scale sensitivities for this equipment are $H = 9 \times 10^{-4}$ gammas at 1 hz and $E = 12.5$ μv/km at 1 km electrode spacing.

Noise power spectral densities for this equipment are shown in Figure 6.

Quoted sensitivities for other magnetometers made for exploration use are in the neighborhood of 10^{-1} gammas full scale for optically pumped devices, and 1 gamma full scale for proton precession and fluxgate magnetometers. Noise levels in each case are 10 to 20 percent of full scale. The flat frequency responses of these other magnetometers gives them the advantage at periods longer than 30–100 sec. Superconducting magnetometers have been built with noise levels comparable to those of the induction coil system described here, but they do not yet seem suitable for use in the field (see Nisenoff, 1969, for example).

From the practical point of view, there are several improvements which would be desirable in present state-of-the-art equipment. Induction coils of adequate sensitivity are clumsy and heavy, and the vertical component coil requires that a hole six ft deep be augered. Several smaller coils in combination might be much more convenient to use. A large loop laid flat on the surface is the only alternative at this time to the vertically emplanted coil.

For work in loose or unsteady surface materials (marsh, ice-floes, loose soil near trees), a system of motion stabilization or compensation would be very helpful.

Hopkins (1965) discusses the engineering and design problems associated with MT instrumentation.

FIELD PROCEDURE

Although basically simple, field procedures require a great deal of planning and attention to detail, since they dominate the costs; and the sensitivity of the measurement makes it highly vulnerable to disturbances at the measuring site.

Two pairs of electrodes aligned at right angles must be laid out at each site, as must three mutually perpendicular magnetometers. A setup is shown schematically in Figure 7. The electrodes provide low resistance, low noise electrical connections with the earth, for the E measurements. The input to each of the E-signal channels is the voltage difference between an electrode pair. (Although one usually thinks of the earth as being at zero potential, voltage differences must exist if telluric currents flow because the earth has a finite resistivity, and $j = E\sigma$.) The farther apart a pair of electrodes, the larger the signal voltage measured, so it is usually desirable to put the electrodes as far apart as possible, subject to

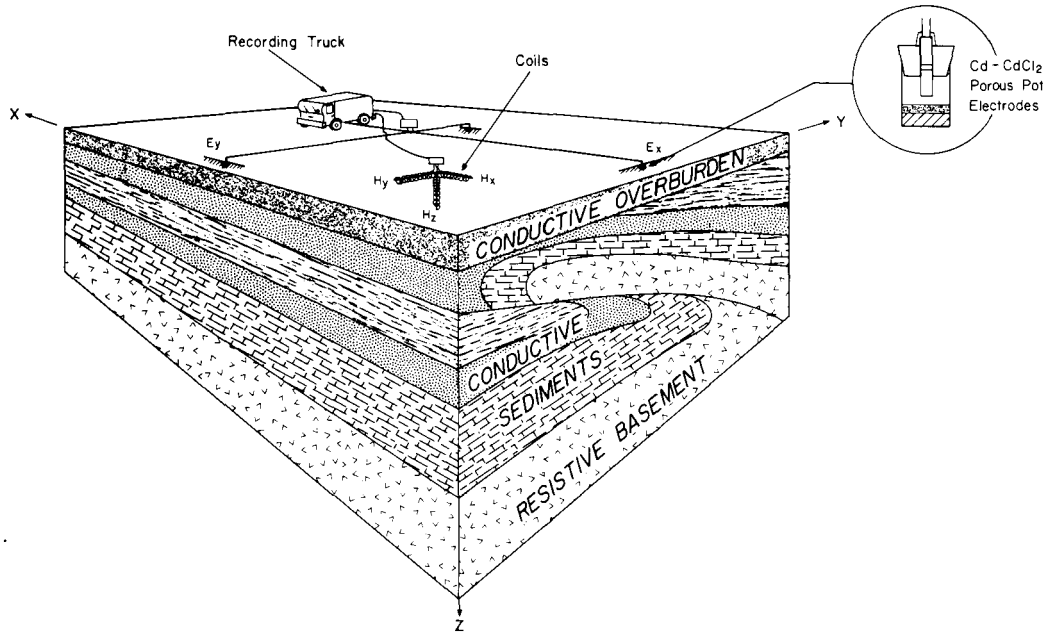

FIG. 7. Field setup.

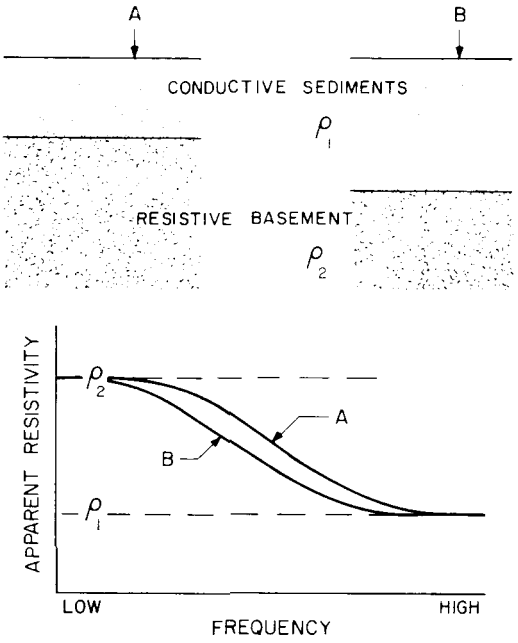

FIG. 8. Diagrammatic two-layer apparent resistivity curves for the models shown.

other factors, such as obstructions, property boundaries, the time needed to lay out connecting wires, and the minimum spacing tolerable between adjacent measurement sites. For routine operations, it is desirable to use fixed wire lengths. Finally, since the wires must not be permitted to move in the earth's main magnetic field as this induces noise, clods of dirt are placed every few feet along the wire to restrain it, a nontrivial task. A 2000-ft spacing is common because it fits conveniently within a quarter section.

The two electrode pairs are intended to measure the two perpendicular components of an electric field vector which exists at each site. However, it is possible for the electric field on the surface to change in both direction and intensity over very short distances, due to large lateral resistivity changes near the surface. Large electrode spacings should be used in this situation to average over as much of the variation as possible, or the resulting data will apply to conditions which are too localized to be of use. For best averaging in these circumstances, it is also important that the two electrode pairs form a cross whose four arms are as nearly equal in length as possible, rather than being arranged to form an **L** or a **T**, (Swift, 1967), and that the coils be near the center.

Topographic features can cause distortions similar to those caused by resistivity heterogeneities. While these can also be modeled, it is better to avoid them if possible, especially if the relief is more than 10 percent or so of the electrode spacing.

Induction coil magnetometers are even more sensitive to motions than are the wires connecting the electrodes. To prevent their moving or vibrating due to wind, the two horizontal coils are buried in shallow trenches 12 to 18 inches deep. The vertical coil is placed in a hole dug by auger. Coils are leveled to within a fraction of one degree by means of sensitive level bubbles. Horizontal azimuth is adjusted to similar accuracy by a simple transit. Burying the coils has the added advantage of reducing thermal transients and the resulting noise. Coils having permeable cores

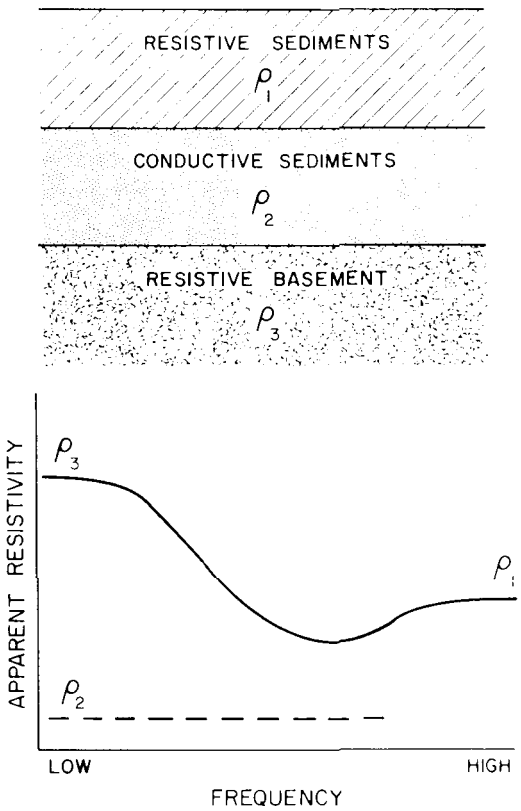

FIG. 9. Diagrammatic three-layer apparent resistivity curve for the model shown.

must be separated from each other by several times their length when they are emplaced, to avoid the effects on each of the local field distortions surrounding the others.

Sites must be chosen with care, to avoid possible sources of disturbance such as cathodic protection circuitry, power and fence lines, unprotected pipelines, and vehicle and pedestrian traffic.

By the use of separate but well-coordinated crews for recording and sensor emplacement, efficient field operations can be achieved. For further efficiency, recordings can be scheduled so as to avoid known or anticipated noise. Customarily, several recordings are obtained in each frequency band, because noise and signal are both variable and largely unpredictable.

DATA ANALYSIS

The purpose of data analysis is to extract reliable values of impedances, apparent resistivities, and the other earth response functions (ERF) from the field records, and to present them in a form convenient for interpretation. Operationally, data analysis consists of (a) manual editing of records, to reject those judged to be contaminated by noise; (b) computer manipulation of tape-recorded data to transform all records into the frequency domain, to derive the ERF which

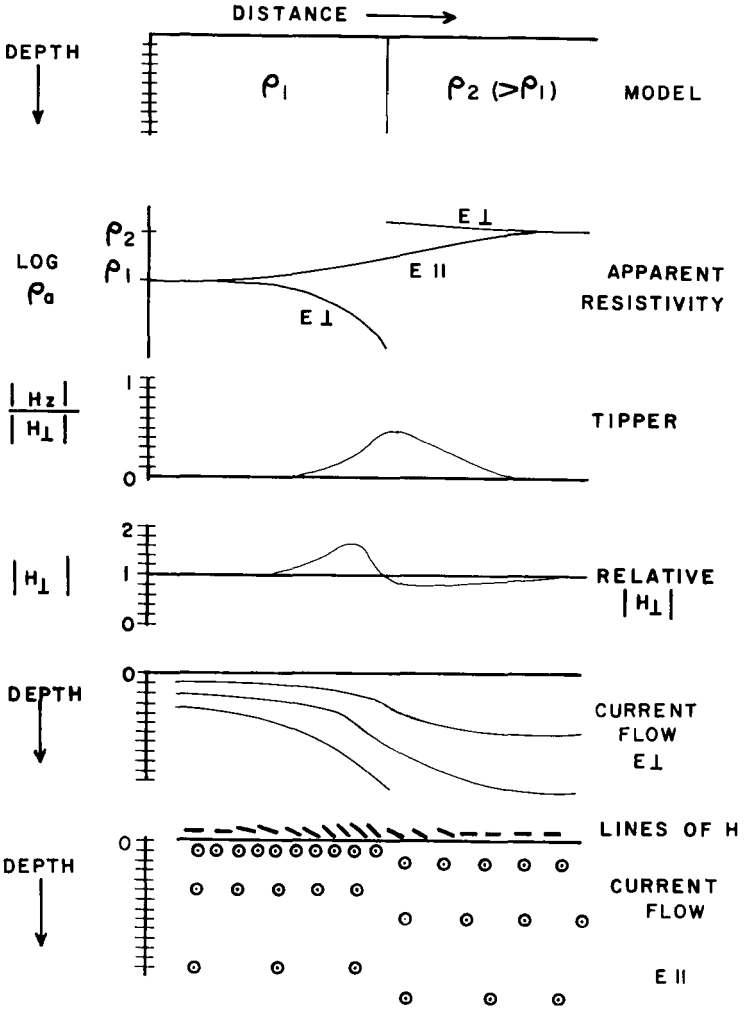

FIG. 10. Diagrammatic response curves for a simple vertical contact at frequency f. Horizontal scales are distance.

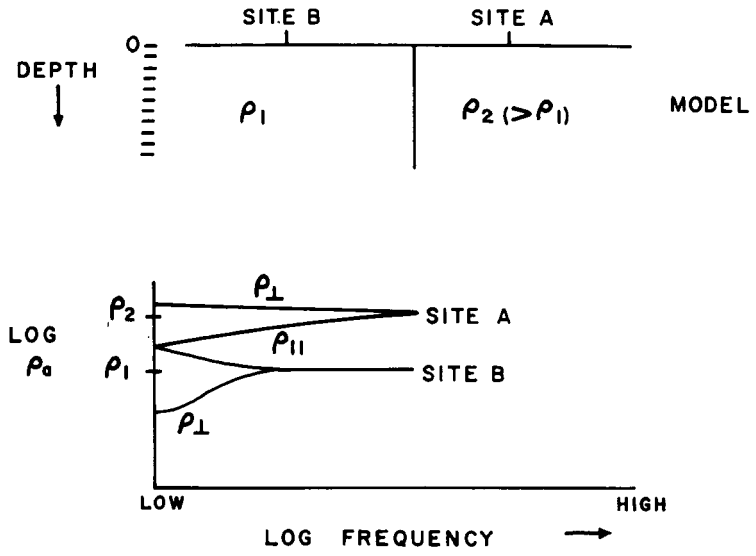

FIG. 11. Diagrammatic response curve for a simple vertical contact. Apparent resistivity versus frequency.

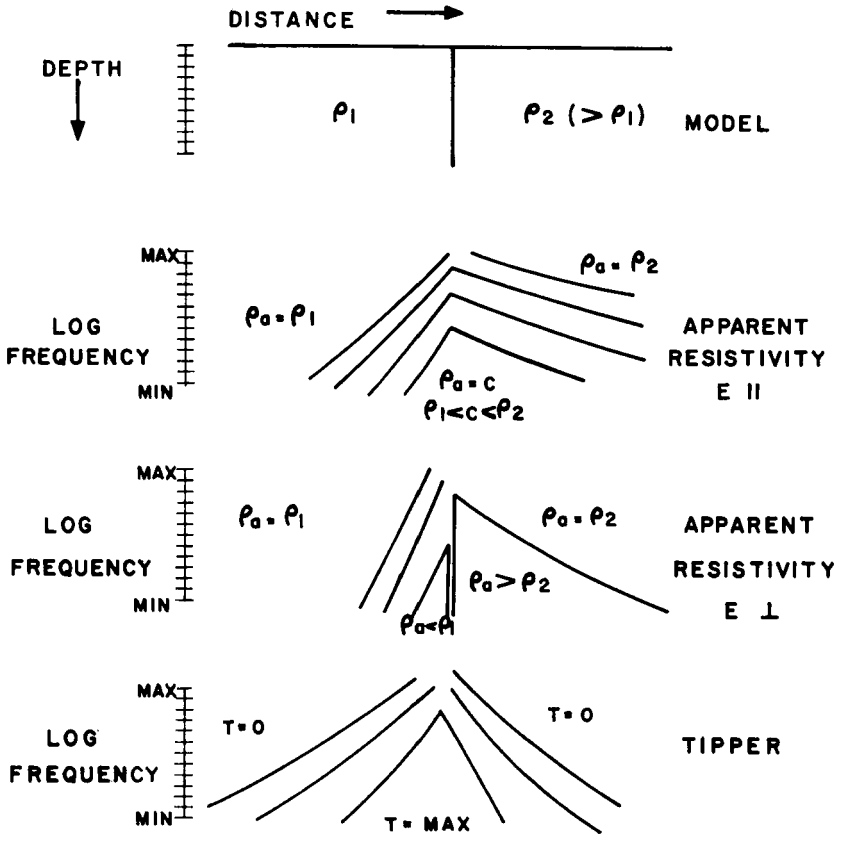

FIG. 12. Diagrammatic pseudosections for a simple vertical contact.

are used for interpretation, to screen each value computed, and to plot in a form convenient for interpretation the values which pass the screening; and (c) manual evaluation of the results so as to reject suspect data and to attempt to extract useful portions of previously rejected data when necessary.

Later, in the interpretation stage, the ERF are compared with those computed for models. These earth response functions are customarily (1) horizontal direction θ_0 of largest apparent resistivity, (2) impedances and apparent resistivities for E in the direction θ_0 and for E perpendicular to θ_0, (3) phases of the two apparent resistivities, (4) the portion of H_z that is linearly related to the horizontal field, (5) the direction of the horizontal magnetic field component most highly coherent with (4), and (6) the phase difference between (4) and (5). Motivation and theory for the first three functions can be found in Madden and Swift (1969), Cantwell (1960), Madden and Nelson (1964), and Swift (1967). Some of the analytical techniques for their computation are summarized and discussed by Sims and Bostick (1969), and Word et al (1969). Motivation and theory for the last three functions are discussed in Vozoff and Swift (1968), Sims and Bostick (1969), and Word et al (1969). Their computation was devised by T. R. Madden and is summarized below. Rankin (1969) and Kunetz (1969) have suggested techniques for and advantages of extracting the ERF in the time domain.

The first phase, manual editing, involves the examination of both recording log books and chart records for evidence that artificial or wind noise is large enough to downgrade a record. Records degraded by noise are not used if their use can be avoided, although it is sometimes necessary to reconsider using their quieter parts when insufficient quiet data exist.

Fourier transformation of each of the five recorded field components is the second step in analysis. This step yields in-phase and quadrature values for each component at as many frequencies as there are samples. The ERF are derived from these numbers..

It is helpful at this point to describe a few of the properties of the ERF, anticipating the section on interpretation, in order to explain some of the procedures which are used in data analysis. In two-dimensional structures when neither of the coordinate axes is along strike, all four elements of the impedance tensor Z_{ij} are nonzero and have different values. Magnetic field components in the x direction give rise to some currents along x, in addition to the y-directed currents, which would be the only ones if the earth were uniform or horizontally layered. Magnetic y components are likewise associated with both E_x and E_y, so that Z_{xx}, Z_{xy}, Z_{yx}, and Z_{yy} will all have some finite values. Now if the coordinate axes are rotated (either physically or by computation) until one of them is along strike, then currents due to H_x can no longer be deflected into the x direction and those due to H_y flow only in the x direction. In this situation, Z_{xx} and Z_{yy} must be zero. The other pair are nonzero and unequal, since current densities will differ in the two directions, and the E components must also differ. If the coordinates are rotated a further 90 degrees, the same situation is found, except that the Z values are inter-

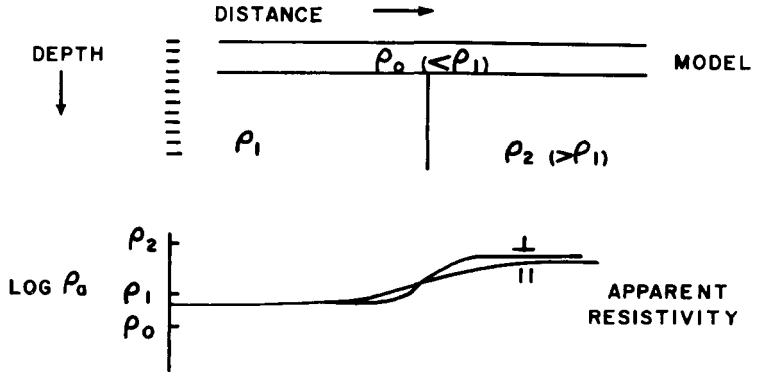

FIG. 13. Effect of burial on the apparent resistivity of a contact. Compare with Figure 10 at the same frequency.

changed. Some of the other properties of the impedance elements are not so apparent. One of these is that

$$Z_{xx} = -Z_{yy} \tag{9}$$

regardless of the angle between the coordinate axes and strike. Equation (9) was also found by computation to be valid for an arbitrary number of horizontal layers, each of which is arbitrarily anisotropic. Another important property is that

$$Z_{xy} - Z_{yx} = \text{constant} \tag{10}$$

at all orientations.

In three-dimensional structures, the tensor elements are still well behaved, according to Sims and Bostick (1969). By plausibility arguments, they arrived at

$$Z_{xx} + Z_{yy} = \text{constant} \tag{11}$$

and

$$Z_{xy} - Z_{yx} = \text{constant}. \tag{12}$$

The Z_{ij} are first found from the transformed data by solving equations (7) and (8). This involves using two equations in four unknowns. The apparent discrepancy is resolved by taking advantage of the facts that the Z_{ij} change very slowly with frequency and can therefore be computed at far fewer frequencies than there are transform values. That is, the Z_{ij} are calculated as averages over frequency bands with each band including many points of the transform. This has been done in a number of different ways, the most common of which is that described by Madden and Nelson (1964). Each equation is written as

$$\langle E_x A^* \rangle = Z_{xx}\langle H_x A^* \rangle + Z_{xy}\langle H_y A^* \rangle \tag{13}$$

and

$$\langle E_x B^* \rangle = Z_{xx}\langle H_x B^* \rangle + Z_{xy}\langle H_y B^* \rangle, \tag{14}$$

where A^* and B^* are the complex conjugates of any two of H_x, H_y, E_x, and E_y, and CD^* is the cross power of C and D,

$$\langle CD^* \rangle(\omega_1) = \frac{1}{\Delta\omega} \int_{\omega_1 - (\Delta\omega/2)}^{\omega_1 + (\Delta\omega/2)} CD^* \, d\omega. \tag{15}$$

Six different combinations are possible, so that six different values of each Z_{ij} can be calculated (H_x, H_y; H_x, E_y; etc). Most commonly, the two H components are used, as they are expected to have a greater degree of independence (smaller cross power) than any other pair. The denominator of each resulting equation is

$$\langle H_x A^* \rangle \langle H_y B^* \rangle - \langle H_x B^* \rangle \langle H_y A^* \rangle. \tag{16}$$

If A and B are strongly dependent, the two terms in the denominator become nearly equal. Although other pairs can and have occasionally been used, the (H_x, H_y) pair is found in practice to give results that are as good or better than any of the others in terms of the numbers of points passing acceptance tests. Exceptions have been observed, particularly when one H channel has been contaminated by artificial noise. The nature of the acceptance tests is discussed below.

Performing the multiplications and solving the equations give the following four expressions to be evaluated:

$$Z_{xx} = \frac{\langle E_x A^* \rangle \langle H_y B^* \rangle - \langle E_x B^* \rangle \langle H_y A^* \rangle}{\langle H_x A^* \rangle \langle H_y B^* \rangle - \langle H_x B^* \rangle \langle H_y A^* \rangle}; \tag{17}$$

$$Z_{xy} = \frac{\langle E_x A^* \rangle \langle H_x B^* \rangle - \langle E_x B^* \rangle \langle H_x A^* \rangle}{\langle H_y A^* \rangle \langle H_x B^* \rangle - \langle H_y B^* \rangle \langle H_x A^* \rangle}; \tag{18}$$

$$Z_{yx} = \frac{\langle E_y A^* \rangle \langle H_y B^* \rangle - \langle E_y B^* \rangle \langle H_y A^* \rangle}{\langle H_x A^* \rangle \langle H_y B^* \rangle - \langle H_x B^* \rangle \langle H_y A^* \rangle}; \tag{19}$$

$$Z_{yy} = \frac{\langle E_y A^* \rangle \langle H_x B^* \rangle - \langle E_y B^* \rangle \langle H_x A^* \rangle}{\langle H_y A^* \rangle \langle H_x B^* \rangle - \langle H_y B^* \rangle \langle H_x A^* \rangle}. \tag{20}$$

Having computed the Z_{ij}, we can then substitute back into equations (7) and (8) to compute values of E_x and E_y. These values, which are predicted from H_x and H_y, have the interesting characteristic that they must be wholly dependent on the horizontal H field. Thus, any differences between the observed E and the predicted E must be due to contamination of either E or H by noise. For this reason, the coherency between predicted and observed E components has proven to be the most sensitive measure of noise available. It is loosely called the predictability. At "normal" sites a predictability of 0.95 or greater is required of an E component as one of the criteria for the corresponding apparent resistivity to appear on the final plots.

Once the Z_{ij} have been found in the original (x, y, z) coordinate system, they can be rotated to any other system (x', y', z') by an angle θ in the clockwise direction. The rotated impedances are

$$2Z'_{xx}(\theta) = (Z_{xx} + Z_{yy}) + (Z_{xx} - Z_{yy}) \cos 2\theta + (Z_{xy} + Z_{yx}) \sin 2\theta, \quad (21)$$

$$2Z'_{xy}(\theta) = (Z_{xy} - Z_{yx}) + (Z_{xy} + Z_{yx}) \cos 2\theta - (Z_{xx} - Z_{yy}) \sin 2\theta, \quad (22)$$

$$2Z'_{yx}(\theta) = -(Z_{xy} - Z_{yx}) + (Z_{xy} + Z_{yx}) \cos 2\theta - (Z_{xx} - Z_{yy}) \sin 2\theta, \quad (23)$$

$$2Z'_{yy}(\theta) = (Z_{xx} + Z_{yy}) - (Z_{xx} - Z_{yy}) \cos 2\theta - (Z_{xy} + Z_{yx}) \sin 2\theta. \quad (24)$$

The principal axes of Z are the values of θ at which Z'_{xy} and Z'_{yx} take on their largest and smallest values, respectively. One way of finding these directions is to compute Z for many values of θ and interpolate to find maxima and minima. It is preferable to use an analytical technique if possible, to reduce computation. However, the only such technique which has thus far been developed does not directly maximize either $Z'_{xy}(\theta)$ or $Z'_{yx}(\theta)$. Instead it solves for the angle θ_0 at which

$$|Z'_{xy}(\theta_0)|^2 + |Z'_{yx}(\theta_0)|^2 = \text{maximum}. \quad (25)$$

Setting the derivative with respect to θ of this sum equal to zero gives (Swift, 1967)

$$\tan 4\theta_0 = \frac{(Z_{xx} - Z_{yy})(Z_{xy} + Z_{yx})^* + (Z_{xx} + Z_{yy})^*(Z_{xy} + Z_{yx})}{|Z_{xx} - Z_{yy}|^2 - |Z_{xy} + Z_{yx}|^2}. \quad (26)$$

This same value of θ_0 also satisfies

$$|Z'_{xx}(\theta_0)|^2 + |Z'_{yy}(\theta_0)|^2 = \text{minimum}, \quad (27)$$

so that in the case of two-dimensional structures the scheme finds the true principal axes. In the three-dimensional case, the method picks a slightly more general maximum, i.e.,

$$|Z'_{xy}(\theta) + Z'_{yx}(\theta)| = \text{maximum} \quad (28)$$

(Sims and Bostick, 1969). The results are seldom shown as impedance values. Instead, the Z'_{ij} are converted to apparent resistivities ρ'_{ij}, with

$$\rho'_{ij} = \frac{1}{5f} |Z'_{ij}|^2. \quad (29)$$

Apparent resistivity has the phase of Z'_{ij}, that is, the phase difference between E_i and H_j.

Four different Z'_{ij} are extracted at each frequency: Z'_{xx}, Z'_{xy}, Z'_{yx}, and Z'_{yy}. The main purpose of analysis and plotting is to permit interpretation, which is now possible only for two-dimensional structures. Hence, only ρ'_{xy} and ρ'_{yx} are routinely plotted, since they are the only two which appear in two-dimensional models. The other pair of elements, ρ'_{xx} and ρ'_{yy}, is also useful in interpreting data from the field. Although ρ'_{xx} and ρ'_{yy} are often small compared with the larger of the others, they are never found to be zero. This fact can be used to judge the degree to which the structure at a site departs from true two-dimensionality. If ρ'_{xx} and ρ'_{yy} are both very small, we have either a well-defined strike or horizontal layers.

As noted above, both $(Z_{xx}+Z_{yy})$ and $(Z_{xy}-Z_{yx})$ are independent of θ, as is their ratio. The magnitude of the complex ratio of the quantities is called the skewness,

$$S = \frac{|Z_{xx} + Z_{yy}|}{|Z_{xy} - Z_{yx}|}. \quad (30)$$

If S is large, structure at the site must appear to be three-dimensional in that frequency range.

An aspect of this method is that it must use a very wide frequency range to be effectively interpreted. Apparent resistivity curves are smooth and regular when they are plotted on log-log scales. Semilog or linear scales give very steep slopes at very low frequencies and uselessly flat slopes at high frequencies. Since Fourier transforms normally appear on a linear frequency scale but interpretation is done on a log-frequency basis, it is helpful to do the integrations of equation (15) with bands whose center frequencies are equispaced on a logarithmic scale. If n such bands are desired in each frequency decade, the ratio of center frequencies of adjacent bands is

$$\log \frac{f_{i+1}}{f_i} = \frac{1}{n}. \quad (31)$$

Bandwidth, in terms of the number of points of the transforms, must also increase with frequency for consistent smoothing on a log-frequency scale. This is the frequency domain equivalent of the time domain constant Q filters used by Swift

(1967). The bandwidth consideration explains the spacing of points on the plot in this and some other papers on MT.

The other ERF are designed to use the vertical magnetic component H_z to help determine which of the two principal impedance axes is the strike direction. At the same time, the remaining ERF aid the interpreter in understanding the cause of apparent anisotropy, point out distant lateral conductivity changes, and often provide additional warning when three-dimensional structural conditions occur. The concept which guides the use of H_z is the same as that behind the AFMAG and some VLF techniques of electromagnetic propsecting at audio and VLF frequencies.

From the field data we want to find the horizontal direction in which the magnetic field is most highly coherent with H_z. In two-dimensional structures that direction will be constant, perpendicular to strike, for reasons discussed in the next section. It is assumed that, if we wished, the measurement axes could be physically rotated at each frequency to find this direction.

The procedure, due to T. R. Madden (1968, unpublished), is to assume that H_z is linearly related to H_x and H_y and to write at each frequency

$$H_z = AH_x + BH_y, \tag{32}$$

where A and B are unknown complex coefficients.

$$\begin{aligned} A &= A_r + iA_i, \\ B &= B_r + iB_i. \end{aligned} \tag{33}$$

Following the derivation of the Z_{ij}, we integrate

$$\langle H_z H_x^* \rangle = A\langle H_x H_x^* \rangle + B\langle H_y H_x^* \rangle \tag{34}$$

and

$$\langle H_z H_y^* \rangle = A\langle H_x H_y^* \rangle + B\langle H_y H_y^* \rangle \tag{35}$$

and solve for A and B. This pair of coefficients can be thought of as operating on the horizontal magnetic field and tipping part of it into the vertical. For that reason, (A, B) is called the "tipper." Its magnitude in each frequency band,

$$\begin{aligned} |T| &= \{|A|^2 + |B|^2\}^{1/2} \\ &= (A_r^2 + A_i^2 + B_r^2 + B_i^2)^{1/2}, \end{aligned} \tag{36}$$

shows the relative strength of H_z. Its phase is

$$\tan^{-1}\left[(A_r^2 + B_r^2)/(A_i^2 + B_i^2)\right]^{1/2}. \tag{37}$$

For a two-dimensional structure striking in the direction $(\phi \pm 90)$ degrees from x, A and B will have the same phasesif we assume noise-free data, so that A/B is a real number and the tipped horizontal component H_ϕ is at an angle ϕ from the x axis, where

$$\phi = \arctan\,(B/A). \tag{38}$$

(It is important in the use of the tipper to know whether the phase difference between H_z and H_ϕ lies near 0 degrees or near 180 degrees, since, for a simple contact, phase at a single site can be used to determine both strike of the contact and direction to the contact from the site.)

In the three-dimensional case, when A and B have different phases, ϕ can be defined in several ways. For example, the definition of ϕ which maximizes the cross power of horizontal and vertical components is

$$\phi_1 = \frac{(A_r^2 + B_r^2)\tan^{-1}(A_r/B_r) + (A_i^2 + B_i^2)\tan^{-1}(A_i/B_i)}{T^2}. \tag{39}$$

This is a weighted average of rotation angles for the real and imaginary parts of the horizontal. Another rotation criterion is maximum coherency of a horizontal component and H_z. Measures of three-dimensionality are the differences between the principal axis direction obtained by impedance tensor rotation and those obtained from vertical-horizontal field relationships. An indicator of the variations in the latter is the tipper skew, defined as

$$\text{Tipper Skew} = \frac{(A_r^2 + B_r^2)\tan^{-1}(A_r/B_r) - (A_i^2 + B_i^2)\tan^{-1}(A_i/B_i)}{T}. \tag{40}$$

Tipper skew is zero if both the real and imaginary parts of H_z are most coherent with the *same* horizontal component, as for two-dimensional structures.

From A and B we can also calculate a predicted H_z, and determine its coherency with the measured vertical component by

$$\mathrm{coh}(H_z H_z^{pred}) = \frac{A^*\langle H_z H_x^*\rangle + B^*\langle H_z H_y^*\rangle}{\langle H_z H_x^*\rangle^{1/2}\left[A A^*\langle H_x H_x^*\rangle + B B^*\langle H_y H_y^*\rangle\right]^{1/2}} \quad (41)$$

Taken together, these quantities describe the relation of H_z to the two horizontal components. They show the importance and locations of lateral conductivity changes and the reliability of H_z for interpretive purposes. For nearly two-dimensional structures, the tipper can be compared directly with the vertical/horizontal field ratios computed for various models. The absence of a significant (i.e., smooth and consistent) tipper permits one to use layered model interpretation with some confidence. The tipper is also a sensitive indicator of certain noise sources.

It has been pointed out on theoretical grounds that tippers could be caused by factors external to the conducting earth. Fortunately for the method, and for several possible reasons, the MT data so far studied by the writer have shown no evidence of tippers of external origin.

INTERPRETATION

The general procedures of interpretation are discussed in this section. Examples of their application to field results will be shown in the following section.

Interpretation consists of three stages. These are (1) a general qualitative overview of the results, (2) fitting layered models at each site, and (3) two-dimensional and three-dimensional interpretation. When properly carried out, this interpretation sequence results in the best possible estimate of conductivity structure within the survey area. In practice, the third stage is often followed by an attempt to assign rock types and a structure to the results, when experience indicates the attempt may be warranted. Interpretation may draw on other sources of information about the area or about similar areas.

Since all geophysical interpretation is based on comparing observed earth response data with model data, this section will begin with a discussion of models. In horizontally layered structures, a single apparent resistivity curve, or its phase, contains all information of significance. Strike and tipper are undefined. Derivation of apparent resistivity and phase curves for the layered model appear in several published references, for example Madden and Swift (1969), Tikhonov (1950), and Wait (1962). Layered model curves can be calculated as accurately as desired, for as many layers as desired, at computing costs of a few cents each. Suites of curves appear in Cagniard (1953), Yungul (1961), and Srivastava (1967).

Figure 8 compares a pair of two-layer models and their idealized apparent resistivity curves. At a sufficiently *high* frequency, the skin depths are small enough that practically no energy penetrates to the basement. Apparent resistivity is therefore asymptotic to ρ_1 at high frequencies and the upper layer is not penetrated. When frequencies are *low* enough, the top layer has little effect and the apparent resistivity approaches ρ_2. The transition with frequency is gradual, so smooth curves result. The greater layer thickness of model *B* requires going to a lower frequency to obtain the same amount of basement influence on the curve.

A typical three-layer curve is shown in Figure 9 for a second layer which is more conductive than the other two. As expected, the curve approaches ρ_1 at high frequencies, drops toward ρ_2 at lower frequencies, and then goes to ρ_3. Although ρ_a never reaches ρ_2, the presence of a conductive second layer is obvious as long as it is not too thin. (Ways of interpreting its thickness and resisitivity are discussed below.) The extension to cases of four or more layers is clear.

The gradual way in which the effect of each layer appears, as contrasted with the abrupt onset of a reflection in a seismic record, characterizes the weaknesses and the strengths of this method. If, for example, the second layer were thin enough, the apparent resistivity curve would go smoothly from ρ_1 to ρ_3: the second layer would not be seen unless it were extremely conductive. On the other hand, this tendency to average together the minor features permits the method to show up weakly systematic variations which might be lost with a higher resolving power. It can be thought of as emphasizing the grosser (longer wavelength) structural features at the expense of the finer details. This characteristic carries over to the two-dimensional case, so that structural features may show up even though traverses do not cross directly over them, justifying large traverse spacings.

Figure 10 shows the simplest two-dimensional structure, the vertical fault. It displays all of the characteristics of more complicated two-dimensional models, but is one of the few for which any theoretical solutions have been found. Consequently it makes a very instructive example.

The gross differences between this and the horizontally layered models examined earlier are that (1) apparent resistivity and phases vary with rotation of measurement axes and (2) the tipper is nonzero. We consider two sites, one on each side of the fault (see Figure 11). When measurement axes at site A are aligned with the structural axes, the two apparent resistivity curves which result are shown (labeled A) in Figure 11. Measurements made at point B give the two curves labeled B. The subscript for each curve refers to the direction of E relative to strike. H_z and the tipper approach zero with increasing frequency at each location. At low frequencies, the tippers at both sites are asymptotic to the same constant values.

When the values of several quantities are plotted versus location along a traverse crossing the fault, curves such as the apparent resistivity, tipper, and relative $|H_\perp|$ of Figure 10 are obtained. The features to note are the following:

1. ρ_a varies smoothly for currents flowing along to strike, but varies discontinuously, with an overshoot, for currents across strike.
2. ρ_a is asymptotic to the appropriate resistivity value at large distances from the fault.
3. H_z is largest near the fault, decreasing smoothly to zero in both directions.
4. The horizontal H component across strike, $H_\perp$, varies significantly near the fault.

Most of these effects can be understood by examining the current flow patterns near the fault in Figure 10. At a large distance from the interface, currents are crowded closer to the surface on the conductive side. Currents across strike must be continuous through the contact, and they adjust smoothly as shown. Far away from the contact, the values of current density and electric field are appropriate to the uniform medium. Approaching the contact from the conductive side, the current density at the surface decreases; hence, E and ρ_a decrease. Although the current densities on the two sides are identical at the contact, the abrupt resistivity change causes an abrupt change in E, and hence in ρ_a. Because current is continuous and $E=j\rho$, E changes in the same ratio as ρ; ρ_a, which depends on E^2, changes as the *square* of the change in ρ.

Currents and electric fields parallel to strike are able to adjust without having to cross the boundary. The parallel E component and the corresponding ρ_a are continuous across the contact, approaching the appropriate uniform earth solution smoothly with distance on each side. However, the current densities change abruptly here, as illustrated, causing a magnetic field that curves around the higher density region. This is the origin of the vertical H component. Direction of largest H in the vertical plane is shown by the lines of H above E current flow.

More rigorously, there will be a vertical H component only if curl E has a vertical component. If y is the strike direction $(\partial/\partial y=0)$, then for currents across strike $(E_y=0)$ the curl of E has no z component. Currents parallel to strike have a nonzero value for $\partial E_y/\partial x$, so they also have an associated H_z component.

When measurements are made along a traverse line as is natural in two-dimensional situations, a more convenient presentation of apparent resistivities than that of Figures 10 and 11 is essential. One such presentation is the pseudosection, suggested by Neves (1957). Figure 12 shows pseudosections for the fault. The horizontal scales are distance; the vertical scales are frequency with lowest frequencies at bottom. Apparent resistivity value is plotted beneath site location at the appropriate frequency for each site, and the results are contoured. Separate pseudosections have to be constructed for E parallel and H parallel to strike.

As a means of further explaining the logical basis of the second stage of interpretation, we will discuss three additional models. These are the buried steeply dipping contact, the thin dipping conductive dike, and the thin dipping resistive dike.

When a cover of resistivity ρ_0 is laid over the previous model, the result is to smooth and attenuate all of the boundary effects which were seen. The degree of smoothing increases with the thickness and conductivity of the overburden (Figure 13). Apparent resistivity curves at large distances from the contact are those of the appropriate two-layer model. The two pseudosections for E parallel and E perpendicular become very similar. Although the transition in apparent

resistivity will still be more abrupt for currents flowing across strike, the actual discontinuity vanishes because both current density and resistivity are continuous. The tipper then becomes a more important clue to strike.

Many faults in older consolidated and metamorphosed rocks have the appearance of narrow conductive dikes. Shale beds, which often are the loci of imbricate faulting, also behave like conductive dikes. A steeply dipping thin conductive dike has a pronounced effect on parallel current and electric field and is therefore effective in generating a tipper. However, the dike's effect on the E field across it does not become large until the dip is very shallow, when the dike starts to behave as a conductive layer. Figure 14 shows the behavior of the dike when it is vertical. The $E_{\parallel}$ apparent resistivity responds at a substantial distance on either side, giving the dike the appearance of a conductive valley. If this actually were a conductive valley, however, the $E_{\perp}$ apparent resistivity would also show it. The lack of response in $E_{\perp}$ is diagnostic of the narrow steeply dipping conductor. The same lack of response holds even for dips as shallow as 45 degrees.

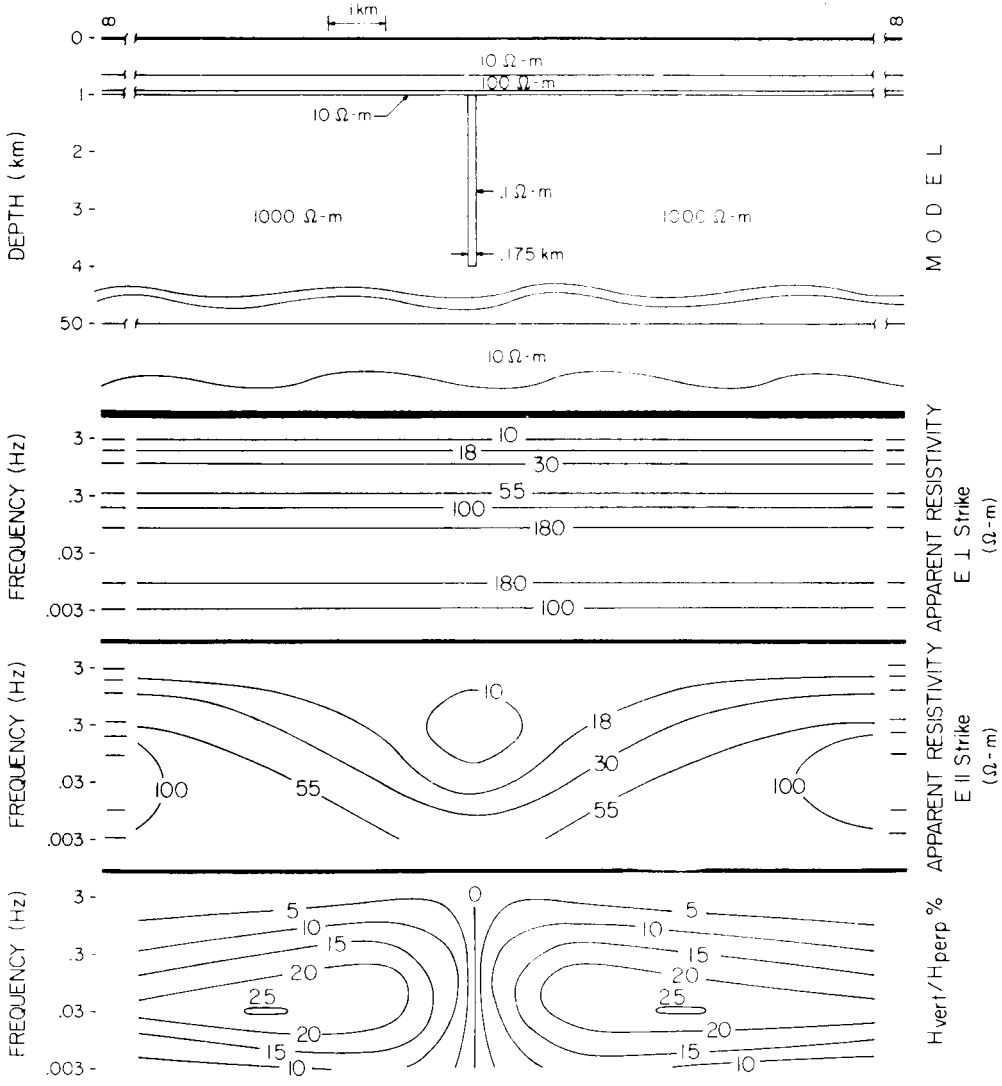

FIG. 14. Computed model of a buried vertical conductive dike.

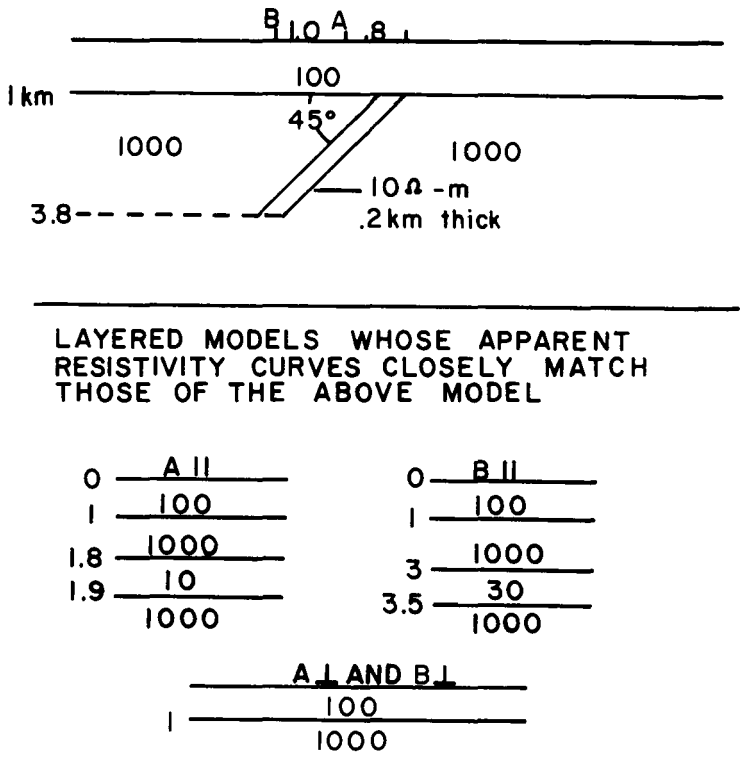

FIG. 15. Result of fitting layered models to response curves of a two-dimensional structure at sites A and B.

The result of fitting horizontally layered models at two locations over a conductive dike is shown in Figure 15. Site A is 0.8 km from the trace of the dike, and B is 1.8 km from the trace. The $E_\perp$ components show no evidence of the dike. In the $E_\parallel$ components, the dike has much the same effect on apparent resistivity as does a conductive layer. If the $E_\parallel$ interpretations were used to construct an electrical cross-section, they would show a conductive bed dipping in the right direction. Although the interpreted thickness and conductivity of the bed would not be individually correct, the conductivity-thickness products would be reasonably close to that of the dike (0.01 and 0.015 versus 0.02).

In the extreme case, many thin conductors in a more resistive matrix cause the material to behave as a uniform but anisotropic material. Such a model can be used to study the effects of dip on apparent resistivities. Figure 16 shows the apparent resistivities for an anisotropic model. In this case, the anisotropy was confined to a second layer, the first and third layers being isotropic and homogeneous. The results further illustrate that the dip must be fairly shallow (here less than 30 degrees) for the thin conductors to have much effect on $E_\perp$.

If the thin dike is more resistive than its surroundings, the situation is reversed: $E_\perp$ apparent resistivity is the component most affected and little effect is seen in the $E_\parallel$ apparent resistivity until the dip is small enough that the dike begins to behave as a resistive layer. This behavior can be seen in the previous (anisotropic layer) model if the 100 ohm-m of the second layer is now considered due to many thin resistive beds in a 10 ohm-m matrix.

The picture just discussed is seen in the immediate vicinity of an isolated resistive dike(Figure 17). Diagnostics are an anomaly in resistivity across strike, with little or no effect on $E_\parallel$ and tipper (not shown). The thin resistive dike seems to represent a fault in young, unconsolidated sediments, as well as salt ridges and intrusive dikes.

It is observed that the $E_\perp$ pseudosections com-

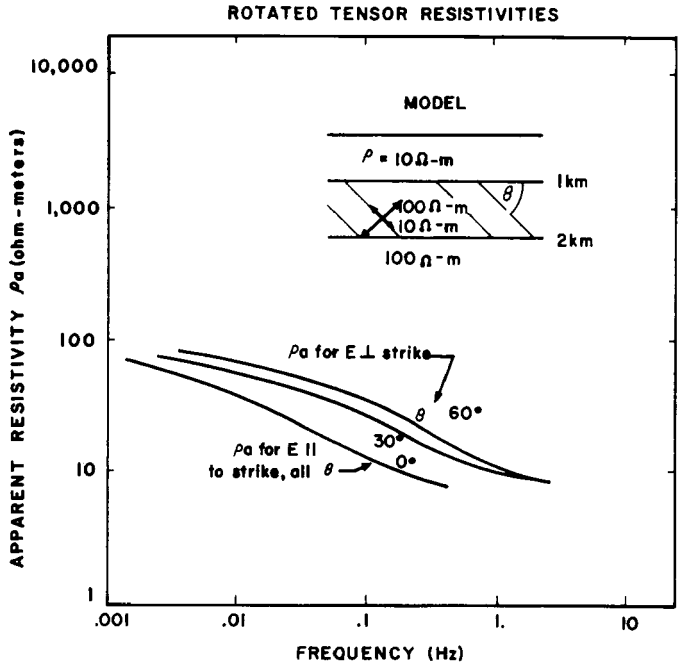

FIG. 16. Changes in apparent resistivity with dip of principal conductivity axis in an anisotropic medium.

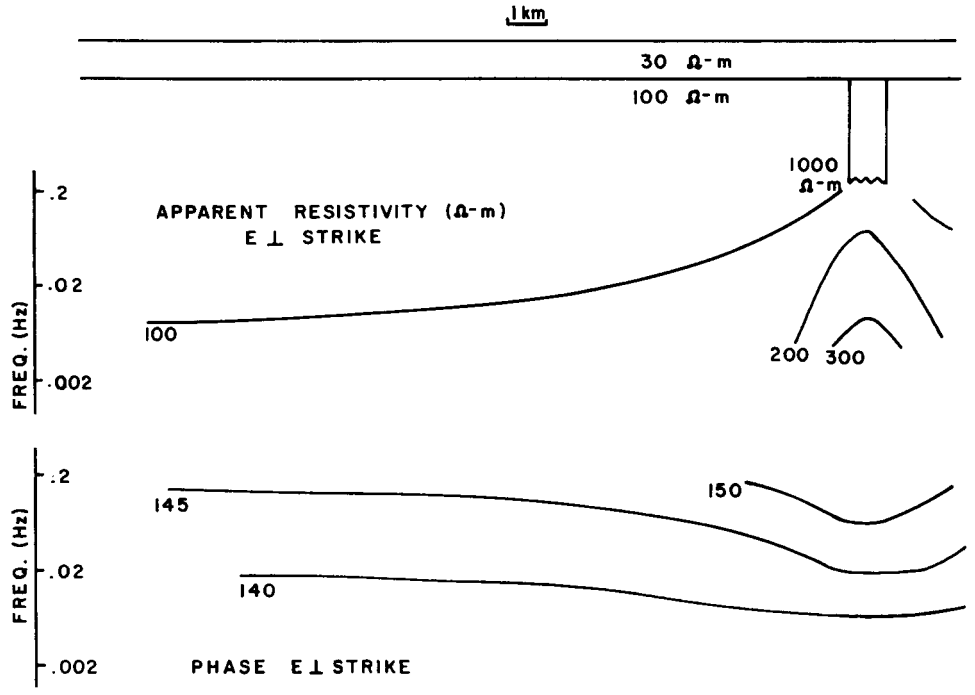

FIG. 17. Computed model of a vertical resistive dike. E∥ resistivity is not distinguishable from that of the two-layer case with the dike absent.

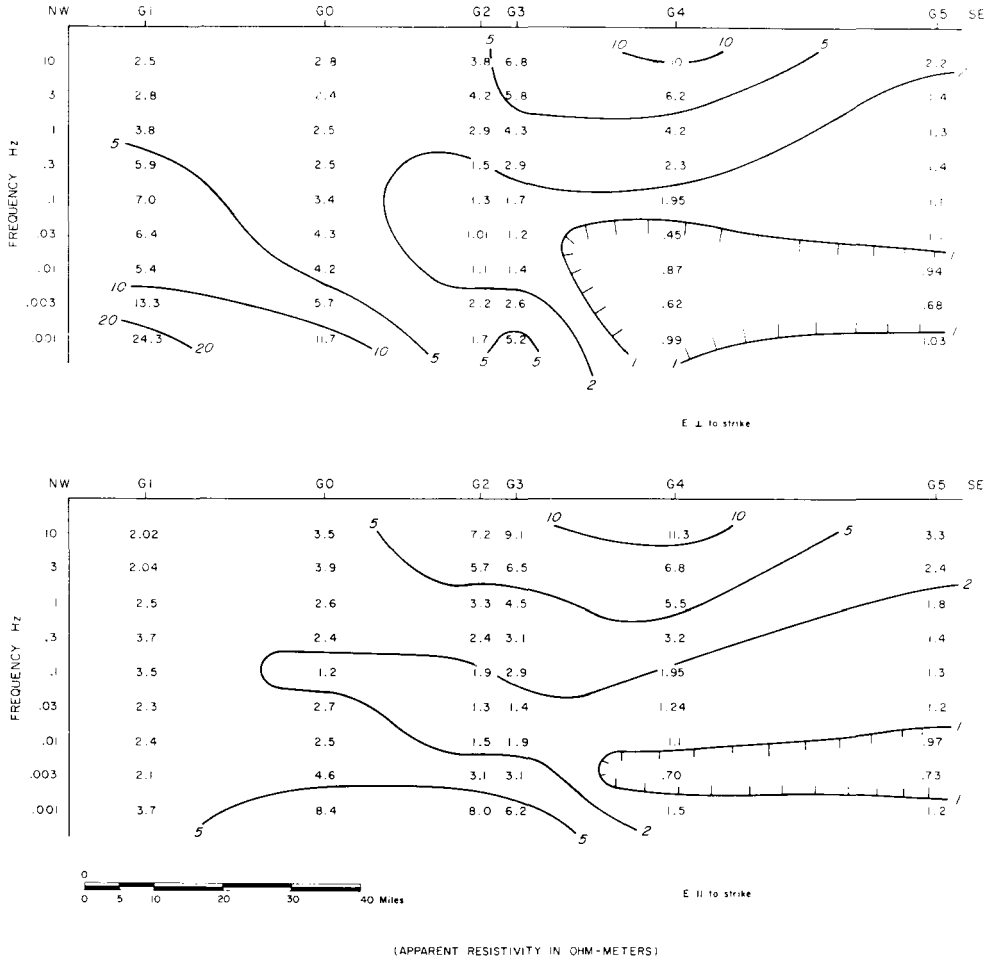

FIG. 18. Pseudosections, South Texas traverse.

monly have a greater range of values and more lateral variation in values than do the $E_{\parallel}$ pseudosections. This is not unexpected, since even in the simplest models the apparent resistivities for $E_{\perp}$ commonly display an overshoot, while a smooth transistion is more typical of those for $E_{\parallel}$. Furthermore, the simplest real earth is far more complex in its variability than any model we might have the incentive to construct, even though there appears to be more regularity to the broad averages for geological units than there is to the fine structure (Keller, 1968; Harthill, 1968). As a result, we are seldom very far from some lateral conductivity change. These two factors explain the larger variance typical of $E_{\perp}$. Any continuity of structure or lithology which may exist is therefore more easily followed in the $E_{\parallel}$ pseudosection, so it is the one most often used for the first (horizontal layer) interpretation. (In the important case in which a narrow resistive structure extends upward into a more conductive section, $E_{\parallel}$ may not resolve the structure and therefore $E_{\perp}$ will yield a better depth estimate on the structure.) If many contours are found between adjacent sites on the $E_{\perp}$ pseudosection, it is taken to indicate a "break" between the sites, and the interpretation is usually confirmed by tipper behavior.

In some areas, the two pseudosections are nearly indistinguishable, indicating no more than gradual changes between sites. In other areas, the two are quite different and change rapidly with location, indicating sharp lateral breaks. Figure 18 shows gradual changes at the south-

eastern end, and apparent anisotropy at the northwest.

Obviously, the smoothness of pseudosections depends in part on the spacing between sites, since even with shallow dips the resistivity-depth curve may change considerably between sites 10 or more miles apart, as in a reconnaissance survey. Here again the tipper can be helpful, since it is found to be negligibly small in the absence of sharp lateral breaks.

If the layered model fitted at each site is extended half way to each adjoining site, we obtain the first-try two-dimensional model. The parameters of this model can then be modified systematically until the pseudosections match the field data. In practice, only a few such trials are usually made because of the large number of variables involved, and the fact that the geology usually departs enough from being two-dimensional that the end result will not be quantitative no matter how good the fit.

Waeselynck (1967) outlined an approach to

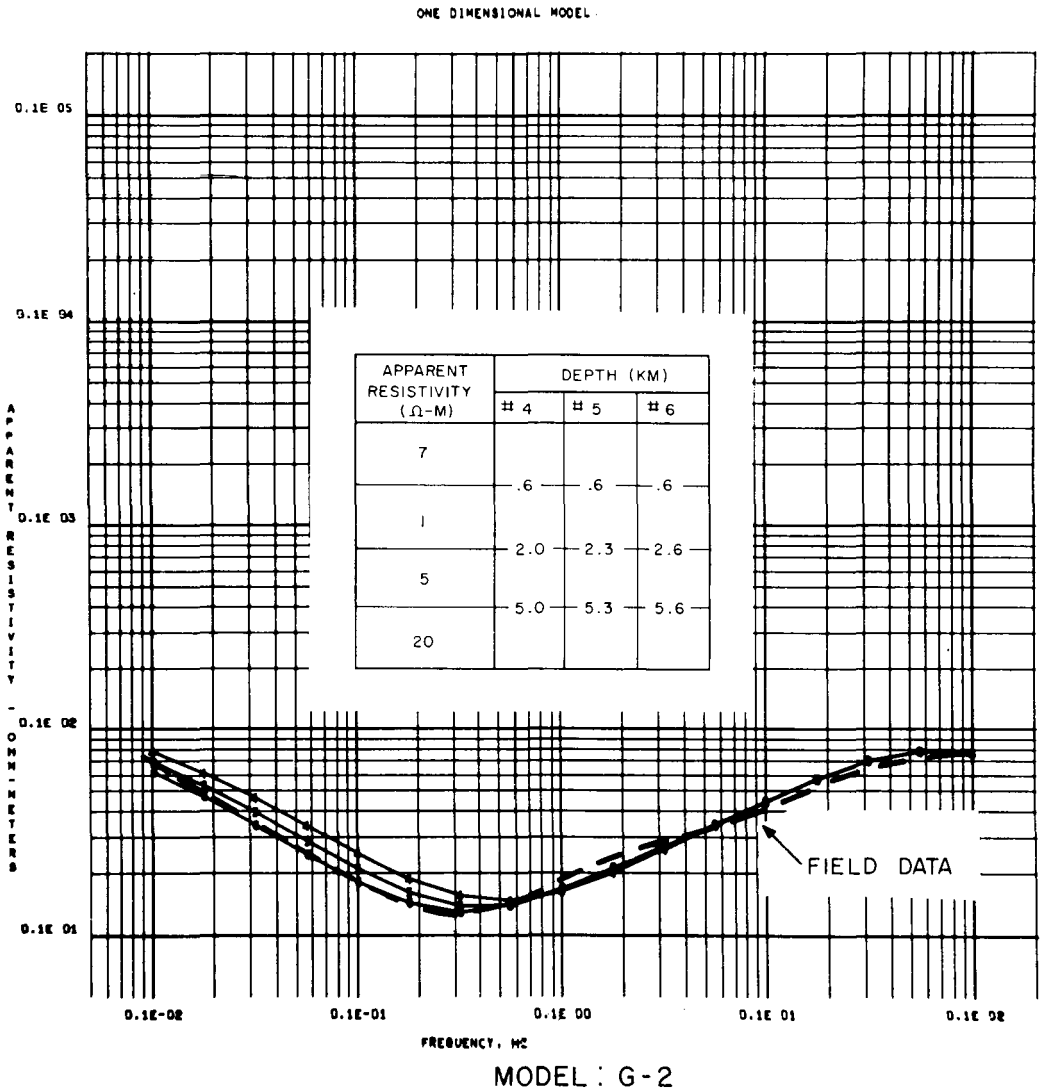

FIG. 19. Cut-and-try layered model fit, South Texas traverse. Model no. 6 fits best the dashed curve drawn through the field results.

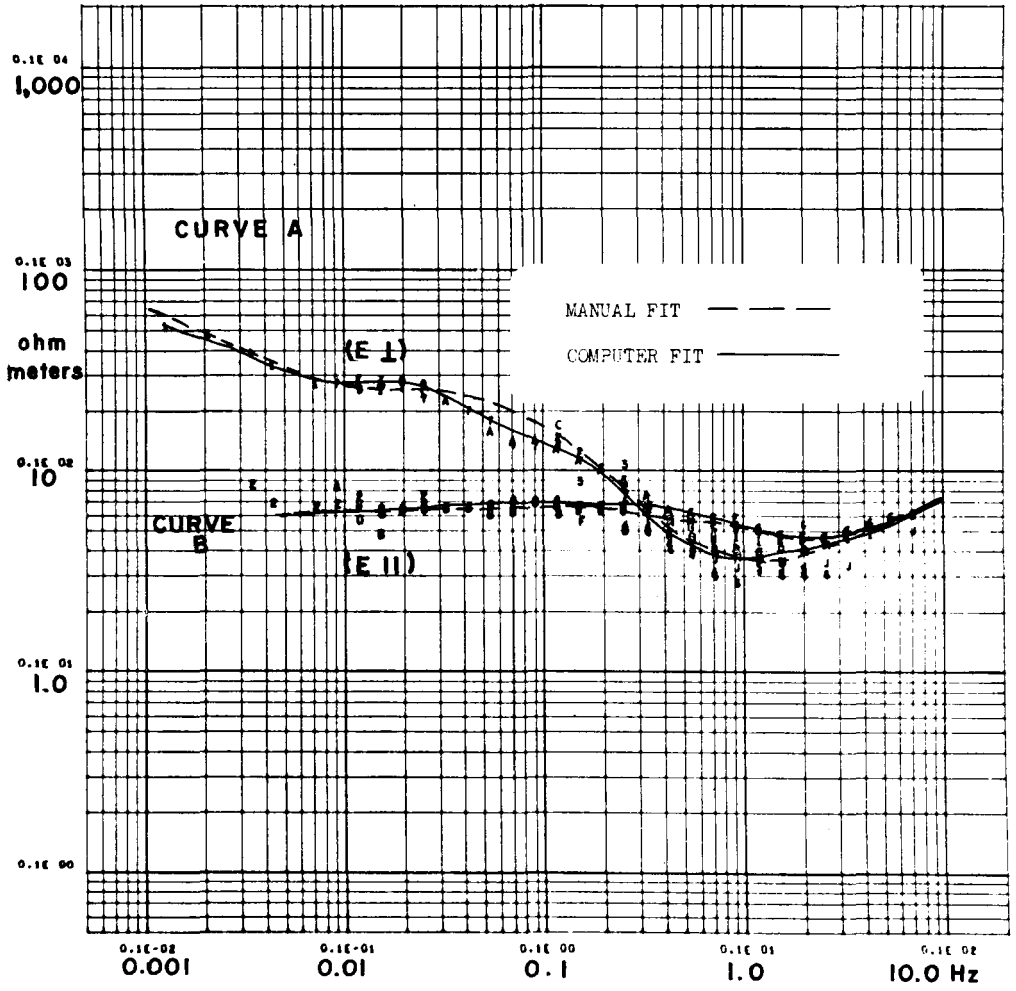

FIG. 20. Interpretation of apparent resistivity data from Oklahoma, showing manually fitted and computer-fitted model curves. Corresponding models are shown in Figure 21.

computing three-dimensional models, but no examples have thus far appeared.

CURVE MATCHING

Most layered model curve matching to date has been done manually, by cut-and-try methods. Numerous sets of computed model curves are available (Yungul, 1961; and Srivastava, 1967) but efficient computer programs for arbitrary horizontal layering are common. Time-sharing systems have been found very useful and inexpensive in this application. An example of a cut-and-try fit is shown in Figure 19.

In addition to the cut-and-try technique, direct computer curve fitting techniques are available. The more common of these use least squares fitting, where the computer attempts to find a model which fits every data point, so as to produce the smallest sum of squared errors (Wu, 1968; Patrick and Bostick, 1969). In the first reference, only apparent resistivity curves are matched, whereas in the second, both apparent resistivity and phase can be fitted.

In least squares methods the number of parameters found (layer thicknesses plus layer resistivities) cannot exceed the number of data points, and all data points used as computer input are usually weighted equally; that is, there is no way to distinguish good data from poor data. More significant, there is no simple, objective

way to tell how good the data are. Indirect indicators are smoothness, predictability, and consistency with time; but these do not distinguish between good one-dimensional data and good three-dimensional data, where the dimensionality refers to the model used to fit the data. The generalized inverse technique, suggested first (in this application) by T. R. Madden and developed by Harter and Madden (in preparation), has the virtue of being able to ignore bad data points, of indicating when the data are otherwise inadequate, and of showing when the model itself is inadequate.

In both manual and direct inversion, the choice of starting parameters can be critical, so that any prior knowledge must be used as early as possible.

To compare the results of curve matching by manual cut-and-try methods with direct (generalized inverse) computer fitting, data were analyzed from a site in the Anadarko Basin. The computer output apparent resistivities are shown in Figure 20. Two curves, the manually fitted

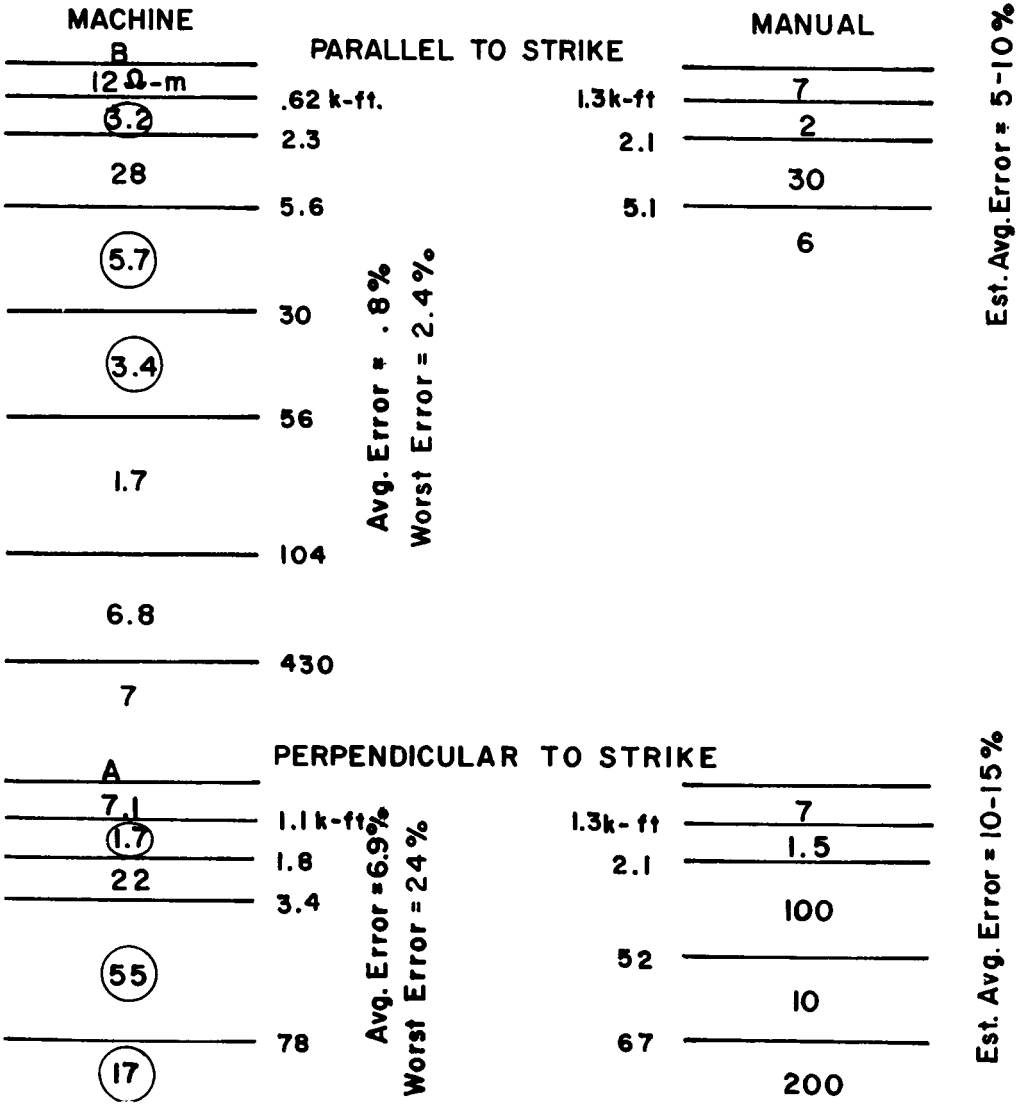

FIG. 21. Models corresponding to the fitted curves of the previous figure. Errors for the manually fitted curves are estimated.

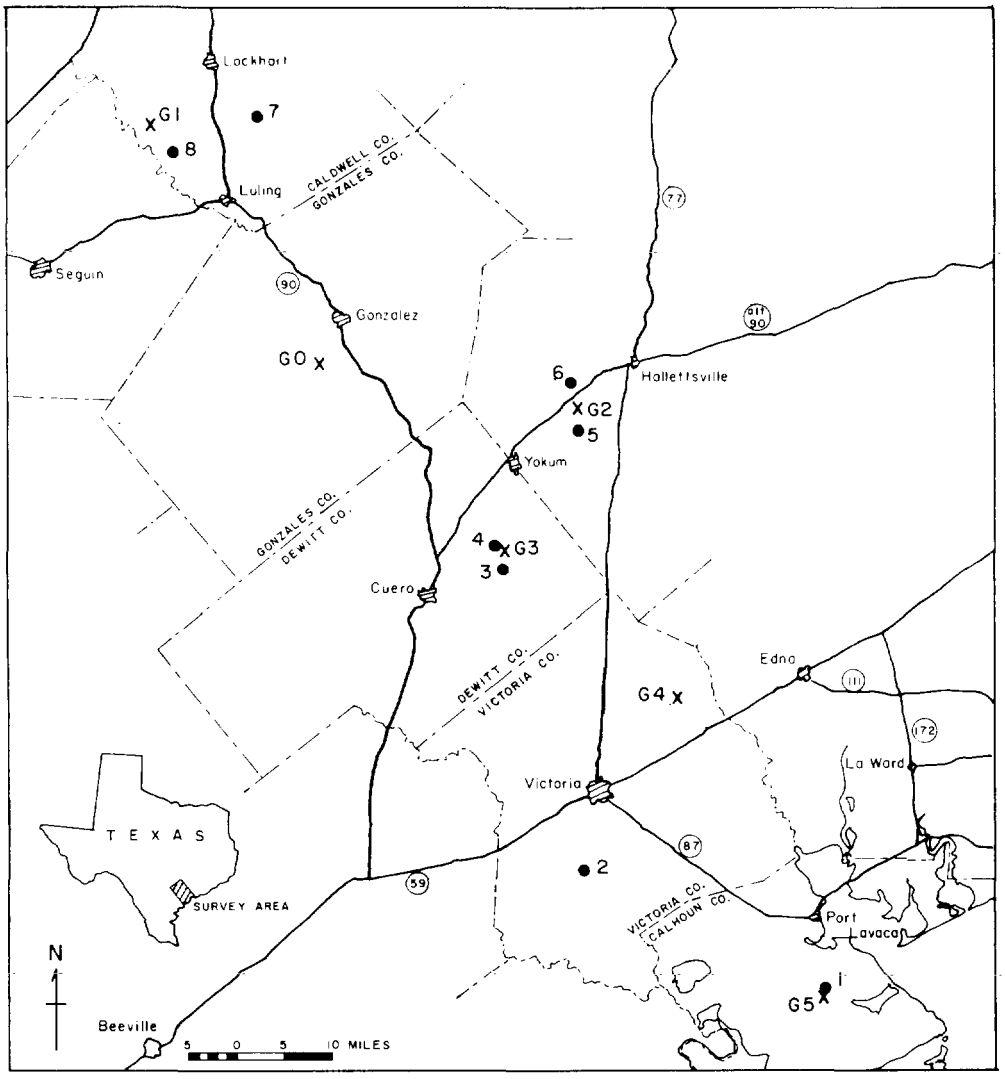

FIG. 22. Location map, South Texas traverse, showing sites and deep wells used for control.

and the direct fitted, are superposed on each set of points; and the resulting models are compared in Figure 21. No error is calculated for the manually fitted curves; in this case, the average error appears to be 10–15 percent for the $E_\perp$ data and 5–10 percent for the $E_\parallel$. The computer fit is obviously closer in each case, but the models are not very different in the upper few thousand feet. Considering the apparent anisotropy, the deeper portions of the models are remarkably consistent with the results to the north, presented in a later section. They indicate the bottom of horizontal layering to be at about 3400 ft subsurface.

The circled values on the machine-fitted models, Figure 21, indicate layers whose parameters are individually best resolved and most stable. These are unlikely to differ much if other starting models are used, for example.

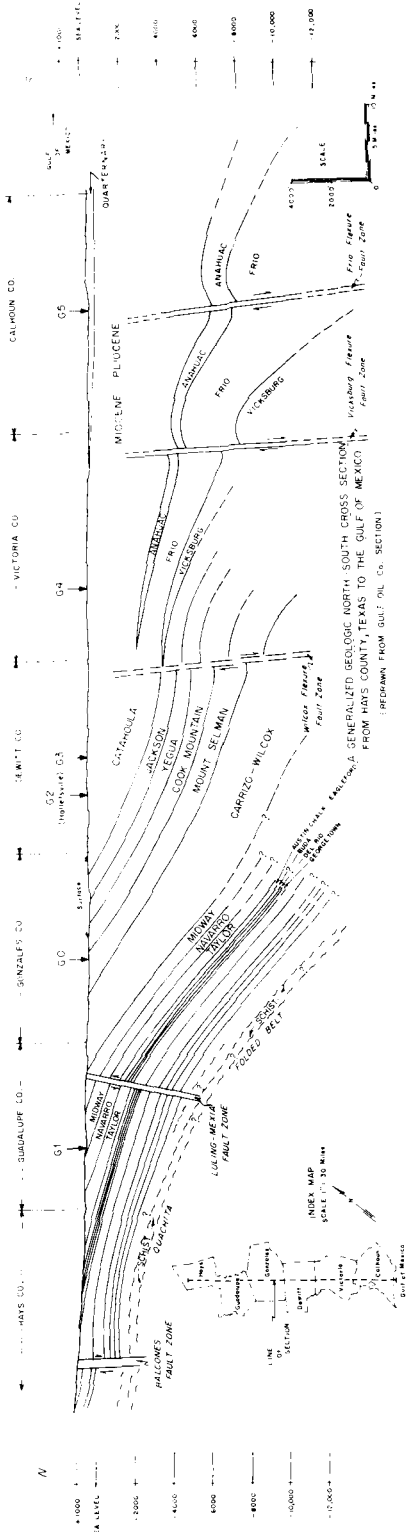

Fig. 23. Geologic cross-section, South Texas traverse.

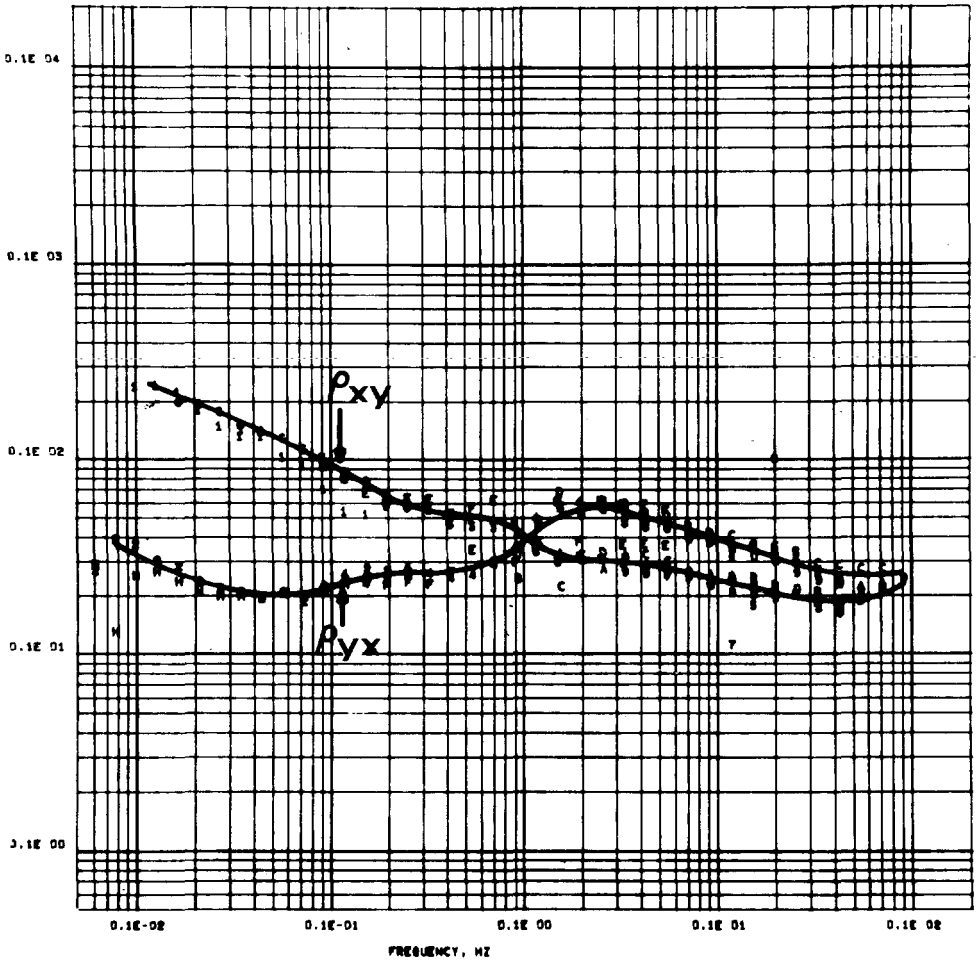

FIG. 24. Rotated apparent resistivities, site G-1, South Texas.

FIELD EXAMPLES

Two examples of the results of field surveys are presented here. One is a wide-spacing reconnaissance traverse in South Texas. The other is an intermediate-spacing traverse in the Anadarko Basin. Both would be considered basin evaluations if they had been carried out in unknown areas. As it is, new data were developed which gave information about the deeper portions of both basins.

South Texas

The first of these surveys (Figure 22) trends northwestward for 115 miles, from Port Lavaca, Texas, on the Gulf Coast to a point 9 miles southwest of Lockhart, Texas. Five magnetotelluric sites were set up along the traverse. One additional site, G-2, was set up 16 miles to the northeast of site G-3 to examine the continuity of data off the traverse. Word et at (1969) have continued MT measurements in the up-dip direction, but their traverse is offset about 40 miles to the northeast.

This area, which is relatively well known geologically, is an important one to the oil industry of the United States. With the good geologic control, it was possible to set up sites such that each succeeding site to the southeast showed the effect of later deposition. Therefore, the traverse enabled us to see, on a gross scale, a magnetotelluric cross-section of the Gulf Coast. We also attempted to detect the presence of high

pressure shales. This area was selected partly because it is open-ended to the Gulf, so that conditions and results ought to resemble those offshore.

The traverse line extended from the flank of the Ouachita folded belt on the northwest, southeastward across the tremendous deposits of Gulf Coast sediments (Figure 23). The line was along the San Marcos arch between the Houston and Rio Grande embayments. The stratigraphic units strike northeast and dip to the southeast. Thus, the traverse extended in a down-dip direction from G-1 to G-5. In general, from northwest to southeast the sites encountered younger sediments and a thickening of the older sediment. Numerous facies changes within the units exist. The traverse crossed a series of the "down-to-the-coast" fault/flexure zones.

Results are discussed first for each site and then for the entire traverse. All apparent resistivities shown have been rotated by equation (26). These data were analyzed before the tipper and direct curve-fitting computations had been started. The vertical magnetic component was analyzed in terms of coherency ratio and phase relative to each of the horizontal component. From these a rough tipper was estimated mentally.

Site G-1

The rotated apparent resistivity curves of Figure 24 indicated that 2-10 ohm-m values predominate beneath this site. Increases in apparent

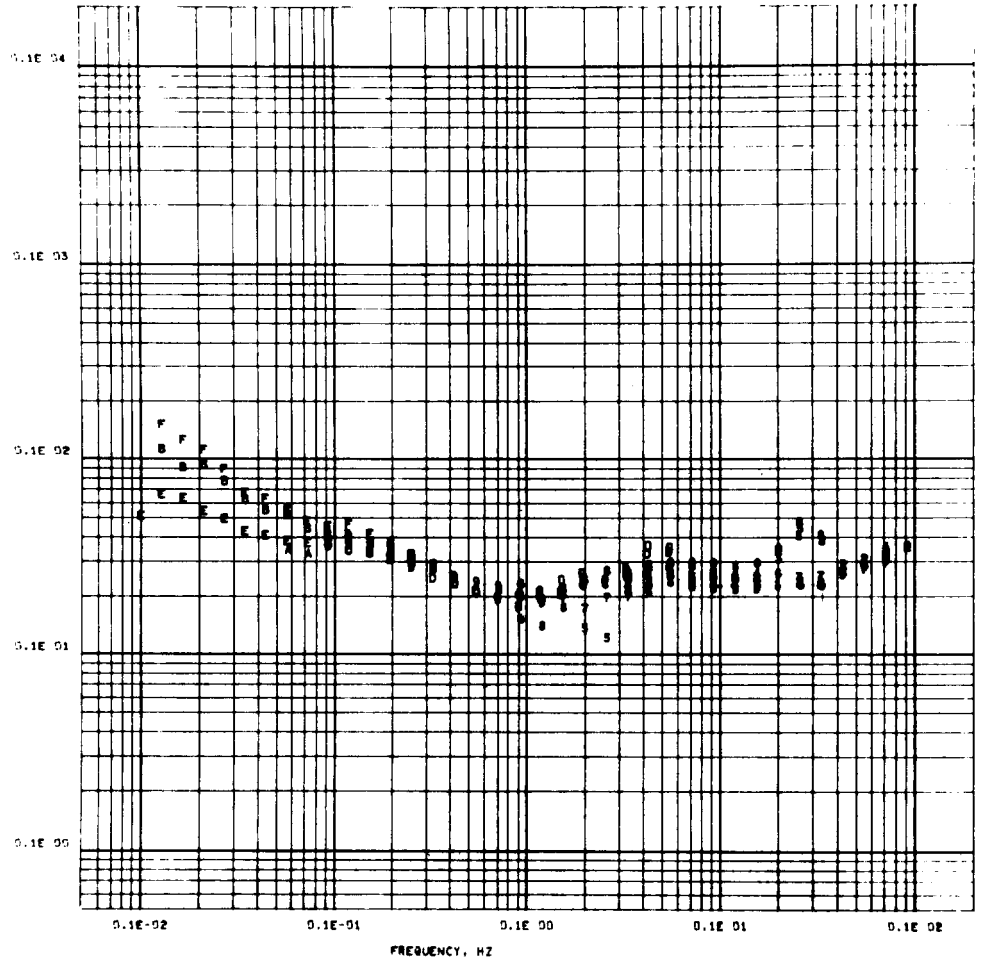

FIG. 25. Rotated apparent resistivities, site G-0, South Texas.

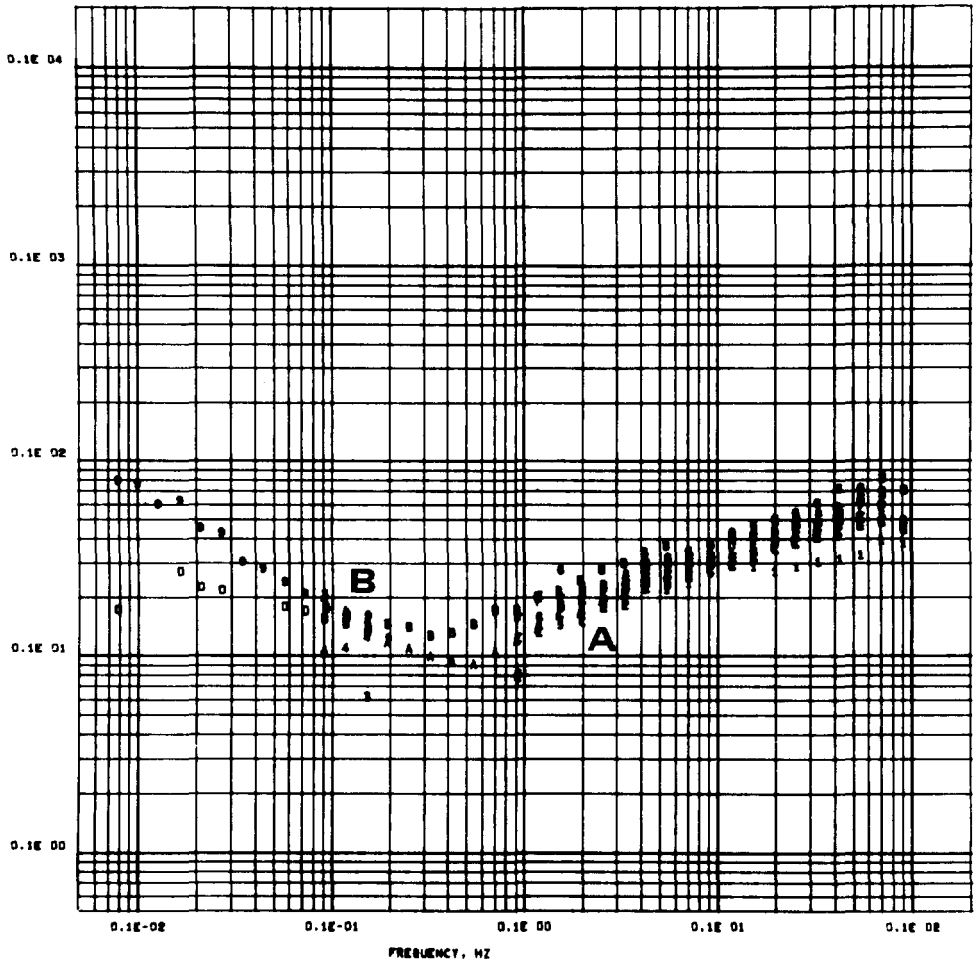

FIG. 26. Rotated apparent resistivities, site G-2, South Texas. E‖ is curve B.

anisotropy with decreasing frequency could be the result of increasing dips, of increasing resistivity contrasts between layers, or both. Pronounced lateral conductivity changes at depths or horizontal distances of 3–5 miles would give similar effects.

Strike at shallow depth is either ENE or NNW, with a 90 degree ambiguity which requires another site for resolution.[1] ENE is believed to be more likely of the two directions. At greater depths, the strike direction is very nearly northward.

Near-surface dips are minor. The data indicate that resistivity may increase slightly toward the east at shallow depth, but below 3000–4000 ft, it increases strongly toward the west. Plot criteria are skew less than 0.2 and predictability greater than 0.95.

Site G-0

Although the rotated apparent resistivities at G-0 (Figure 25) were similar to those at G-1, apparent anisotropy (i.e., the gap between sets of points) is much smaller at G-0. Another major difference between the two sites is the greater thickness of moderately conductive material at G-0. These two observations are reflected in the smaller vertical magnetic field component H_z and the smaller skew at G-0.

Apparent electrical strike direction is definite

[1] Choose one of the directions as strike and set another site several miles away along that direction. If the choice is correct the two sets of results will be very similar. If not, a difference will be observed.

from 0.05 hz downward, varying from N30W at 0.05 hz, to N50W at 0.005 hz and back to N30W at 0.001 hz, with the 90 degree ambiguity throughout. Regional geology suggests that true strike is at 90 degrees to these directions. Resistivity in the uppermost several thousand feet appears to increase eastward.

Sites G-2 and G-3

As shown on the location map, G-2 is 16 miles off the traverse line to the NE from G-3, along what was believed to be regional strike. Results at the two sites differed in some important features, with those from G-2 being the more complex (Figure 26). Apparent anisotropy at G-2 is better developed, rotation angles are more definite, and skew is generally larger except at the lowest frequencies. Below 4000–5000 ft at G-3 (Figure 27) there is a pronounced resistivity increase to the NW. This may continue northeastward past G-3, but is not as clearly indicated there. According to the phase information (not shown), the low frequency apparent resistivities at G-3 rise to larger values than those at G-2 before starting to decrease again. Hence a thicker, more resistive section is expected at depths of 25,000–30,000 ft beneath G-3.

Apparent electrical strike is N70W to N85W at G-2, and probably indicates a real strike direction of N5E to N20E. The apparent electrical strike at G-3 alternates randomly between these same two values. For a shallow strike direction of N5–10E, G-2 should be projected farther to the SE on the interpreted resistivity cross-section, although its

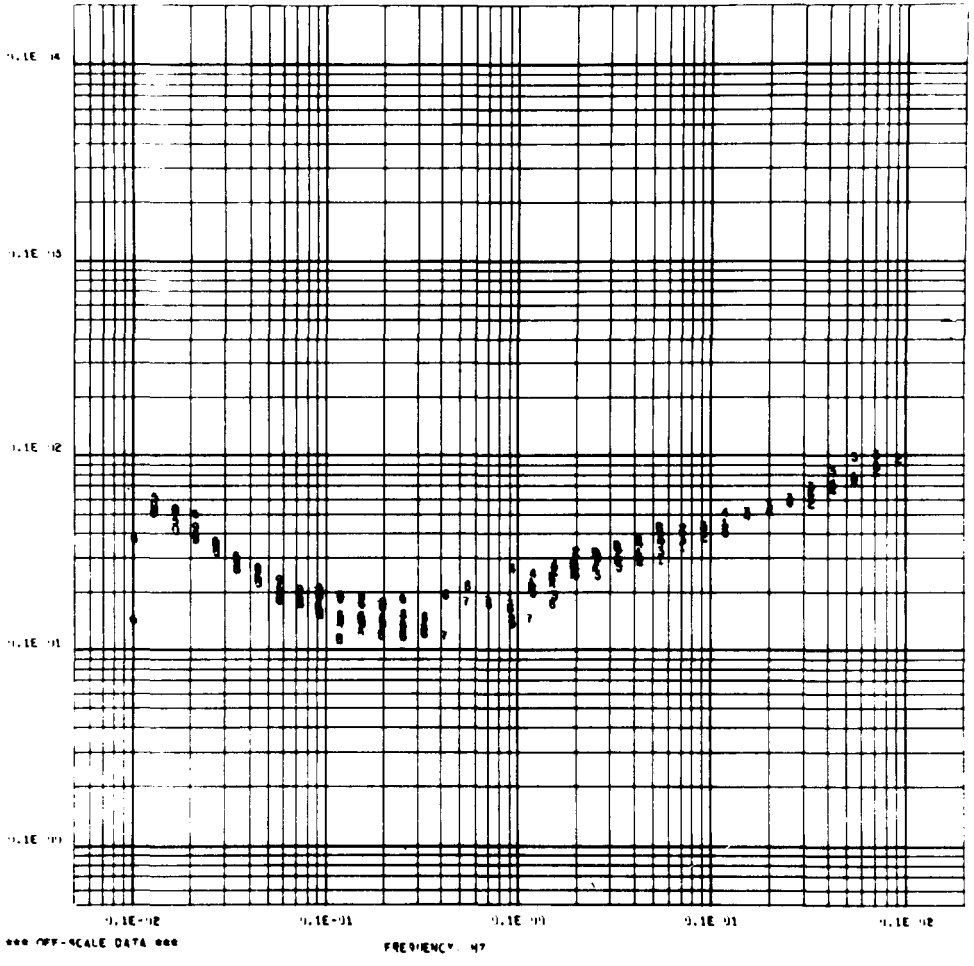

FIG. 27. Rotated apparent resistivities, site G-3, South Texas.

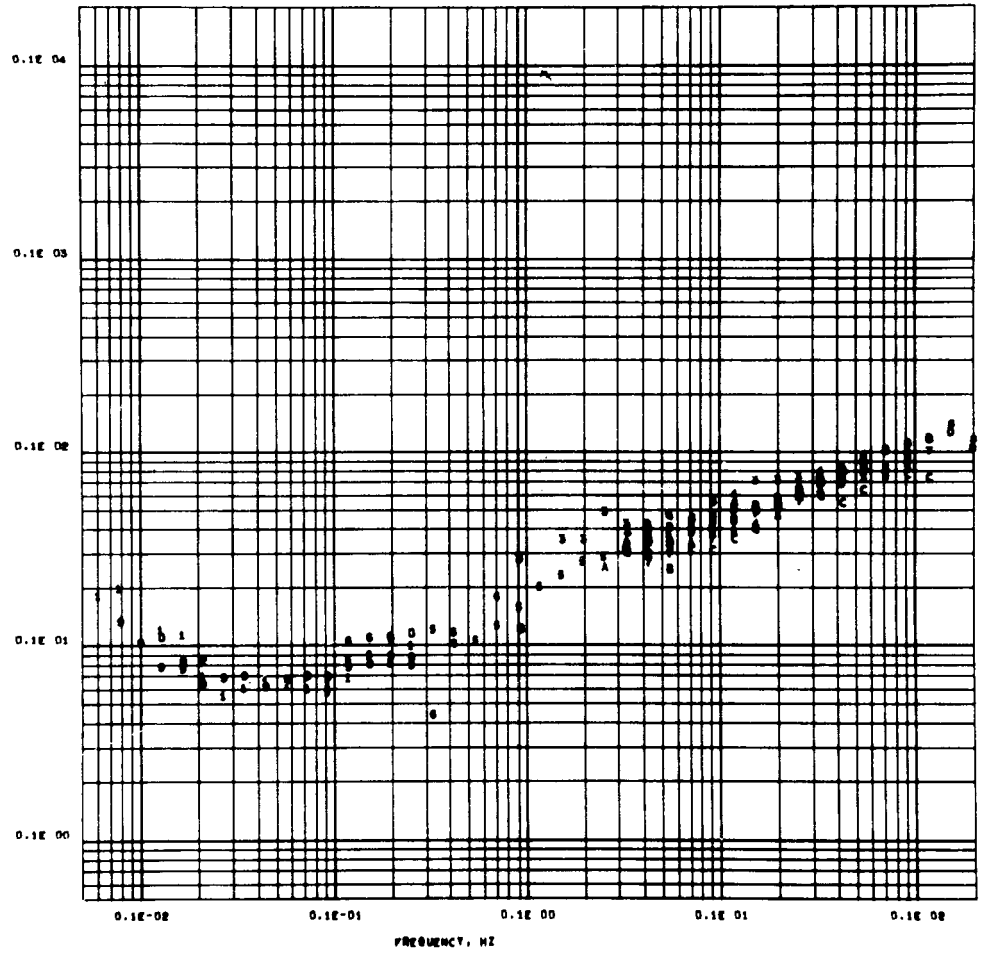

FIG. 28. Rotated apparent resistivities, site G-4, South Texas.

projection is correct for the deeper strikes. Plot criteria are skew less than 0.2 and predictibility greater than 0.85 (G-2) and 0.95 (G-3).

Site G-4

Apparent resistivities (Figure 28) decrease very gradually before rising sharply at 0.002 hz. Apparent anisotropy is minor; apparent electrical strike direction is poorly defined but changes smoothly with frequency from N20W (low frequency) to N10E (high frequency). Noise is large and few low frequency points of ρ_{21} are passable. Plot criteria are skew less than 0.5 and predictability greater than 0.85.

Site G-5

Anisotropy is about the same order as the scatter in the data, about ± 5 percent over most of the frequency range (Figure 29). Rotation angles are poorly defined except at the highest frequencies.

The most unusual aspect (not shown here) of the G-5 data are large values of H_z at the higher frequencies, decreasing linearly with decreasing frequency and closely correlated with H_y. The H vector in the y-z plane is tilted downwards to the east, indicating a north–south conductor lying near the site and to the west of it. This may be caused by an unseen pipeline. An alternative explanation involves near-surface salt-water invasion to the west, possibly as a result of locally enhanced porosity. The University of Texas data at Port Aransas to the south and west of G-5 have high frequency apparent resistivity less than 1

ohm-m (Smith, 1968). Plot criteria are skew less than 0.5 and predictability greater than 0.95.

Traverse

Layered models were matched to each of the $E\|$ apparent resistivity curves by trial and error; and a correlation between stations was carried out, with the result shown in Figure 30. These correlations are obviously open to question and adjustment in view of the large spacings between sites.

The interpreted resistivity section shows three ranges of values: 0.5–3 ohm-m, isotropic; 4–10 ohm-m, isotropic; and >2 ohm-m, anisotropic. The last category is predominant at depth, particularly in the north-west near the thrust. The anisotropy was interpreted as due to dipping or monoclinally folded beds of alternating resistive and conductive materials. Bands of graphitic or black shaly materials, which could provide the lower resistivity value, have been observed in and beneath the thrust zone, both in East Texas and in the exposed Precambrian near Llano. Going from NW to SE, these materials become buried beneath an increasing thickness of the conductive isotropic rocks and, in particular, by a zone of nearly isotropic 0.6–2 ohm-m resistivity. Minor apparent anisotropy, indicating minor dips with small true anisotropy (probably interbedded sands and shales), persists through the entire traverse. The computed resistivity rotation angles and skews suggest that these dips are due to minor local structure, and that it might be possible by careful model work to interpret strike

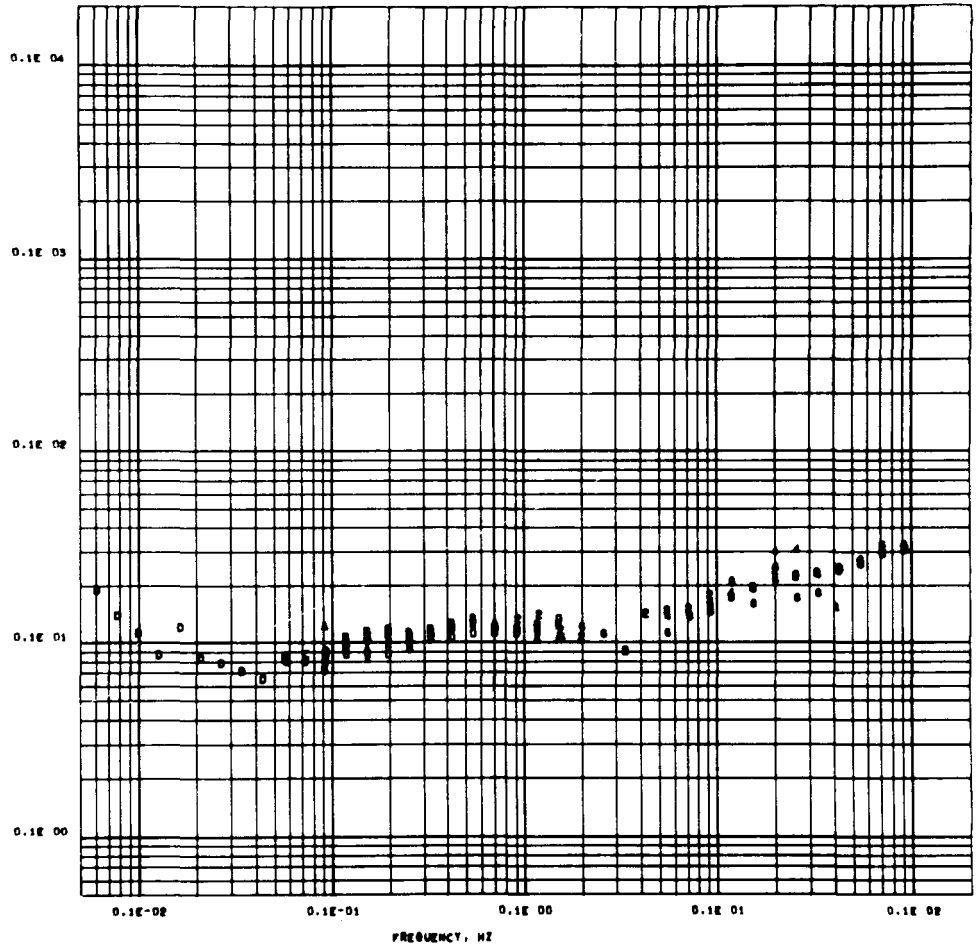

FIG. 29. Rotated apparent resistivities, site G-5, South Texas.

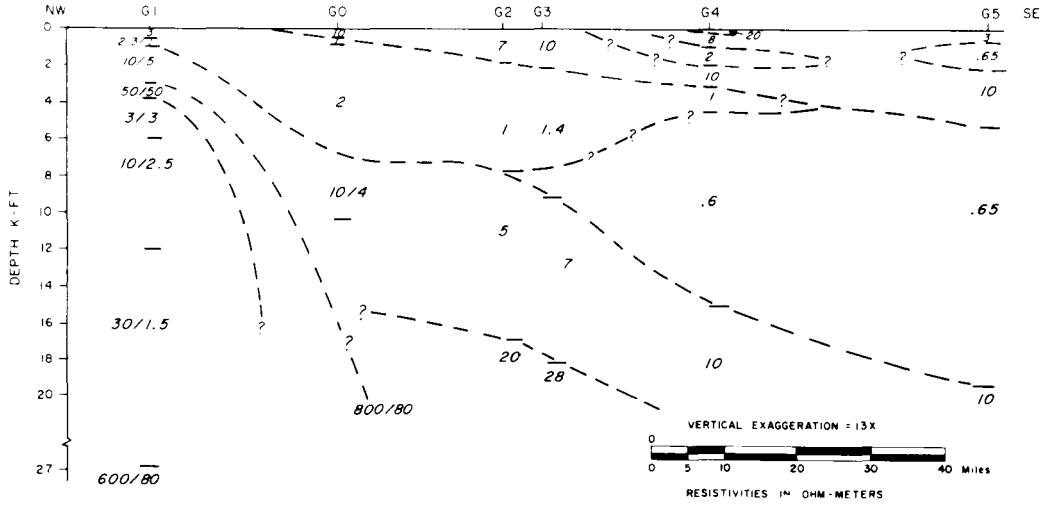

FIG. 30. Interpreted resistivity cross-section, South Texas traverse.

and dip variations with depth beneath the site. The resemblance between this figure and the generalized geologic section (Figure 23) is unmistakable.

There are some interesting differences which appear to be significant. For example, the tendency of the resistivity boundaries to be more nearly horizontal than the geological boundaries appears to be real, and may be a result of water and clay distribution and of compaction. Resistivity in the Eocene decreases systematically seaward, possibly because of a systematic increase in clay content. It has been suggested that the 10 ohm-m material near the surface indicates fresh water invasion.

One of the targets chosen was high-pressure shale, i.e., a shale having a resistivity substantially less than 1 ohm-m, which was known to be present in large amounts beneath G-4 and virtually absent beneath G-2. The apparent resistivities at G-4 and G-5 could not be matched without the thick 0.6 ohm-m zones. No amount of reinterpretation can modify the basic result. The method is unable to resolve the fine structure of the interbedded sands within the overpressured zone, but is able to map features beneath it.

The limited contrasts and simple structure permit us to evaluate resistivity with what is still a surprising amount of resolution. In such situations MT takes on the aspect of a regional stratigraphic tool.

Upon completion of the interpretation, logs from various drill holes along the traverse were obtained and compared with the interpreted section. The location of the drill holes relative to the sites is shown in Figure 22. The comparison of electric log information and interpreted structure is shown in Figure 31.[2] For this example, the electric logs were subdivided by hand into segments, each segment being given the average conductivity for its depth range. A segment then represents a layer. Overall, the agreement is quite good. Disagreement at D.H. 6 (bottom) is within the limits of accuracy; D.H. 7 is further from G-1 than is D.H. 8 and probably reflects lateral variations in near-surface structure. The discrepancy between D.H. 3 and the interpreted section at G-3 may be related to the age of the log (1949).

A more detailed interpretation was carried out at one location, while testing the direct model fitting program. The program uses the generalized matrix inversion program developed by R. Harter and T. R. Madden (in preparation). The results, comparing G-2 and D.H. 6, are summarized in the four curves of Figure 32. The heavy solid curve is the result of smoothing the induction log for D.H. 6 (No. 1 J. Orsak, Mobil Oil Co., 1960–61, mud resistivity = 0.4 at 108 degrees) over steps of 10 percent of depth. The dashed curve is a portion of the four-layer model which was pre-

[2] Induction logs commonly use millimhos/meter (mmho/m) as units of measure. To convert, 1 mho/m $= 10^3$ mmho/m.

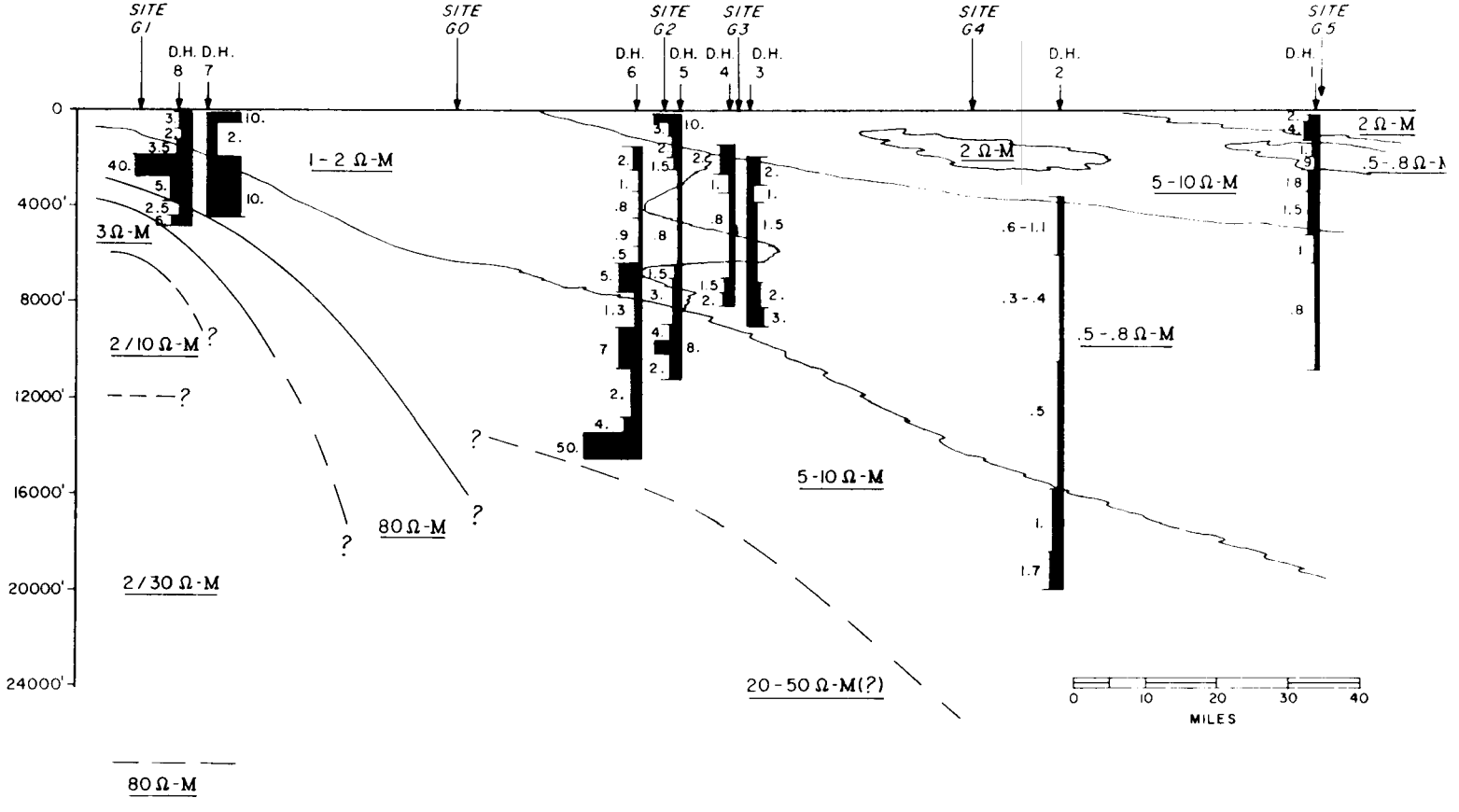

FIG. 31. Comparisons of digitized well logs with models fitted manually. Well locations are shown in Figure 22.

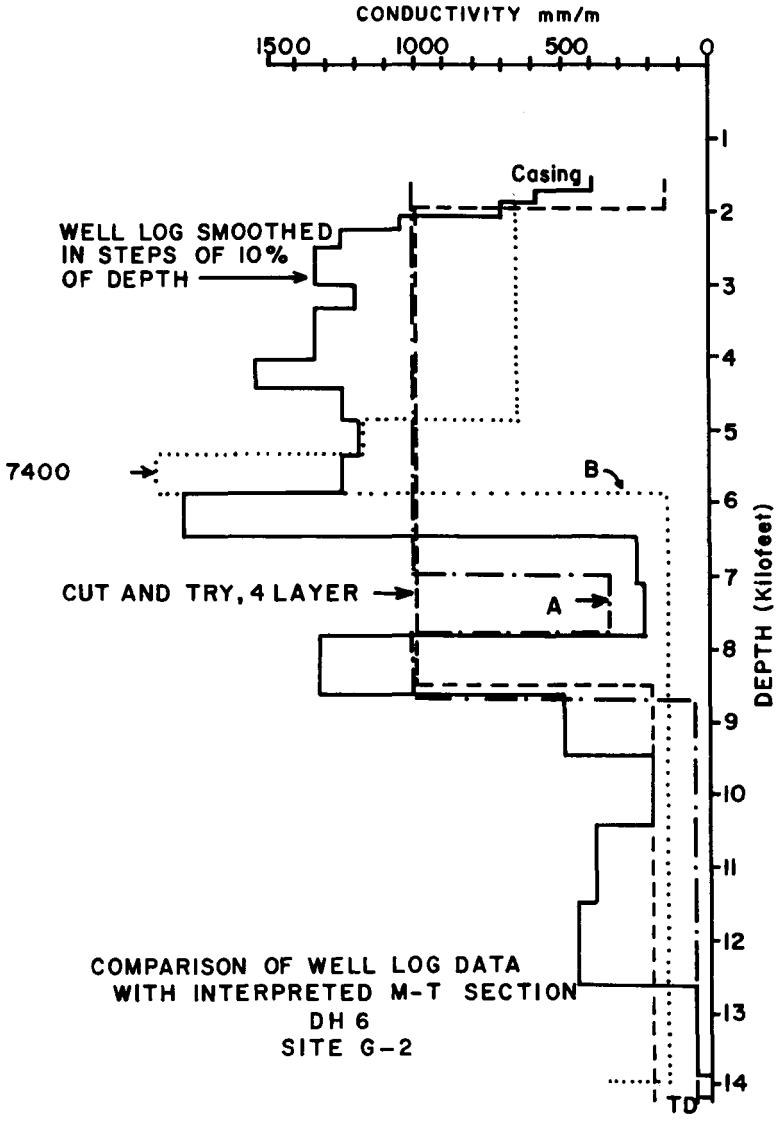

FIG. 32. Detailed comparison of digitized well logs with direct computer interpretations at site G-2. Conductivity is in millimhos/meter.

viously fitted by cut-and-try for $E_\perp$ (curve A, Figure 26). It can be seen to fit the major features of the smoothed log rather well, especially the breaks near 2000 ft and 8500 ft. The significant low conductivity zone from 6500–8000 ft was missed, and conductivity was underestimated in the thick conductive zone from 2000–6500 ft. The two direct-fit models labeled A and B are for the two apparent resistivity curves at the site, B being a fit to $\rho_\parallel$. Six-layer models were used in which both layer thicknesses and their resistivities were permitted to vary. These early inversion results were considered encouraging.

Anadarko Basin

The second field example is a traverse across a portion of the Anadarko Basin, Oklahoma. The basin has an area of approximately 35,000 square miles in western Oklahoma, the northern part of the Texas Panhandle, and southwestern Kansas.

In terms of its depth and volume, it is one of the major crustal features of North America (Basement Map of North America, 1967). Despite its long history of oil production, the Anadarko Basin is currently the site of intensive exploration and some of the deepest drilling in the world. A location map showing our traverse appears in Figure 33. A geological cross-section showing the general basin configuration is shown in Figure 34. This section was constructed from data which are not as recent or as closely controlled as might be desired, but which seem to be the best available.

At the southern end of the traverse are the Wichita Mountains, consisting of Cambrian rocks of the Wichita granite group. Immediately to the north where the basement is still near-surface,

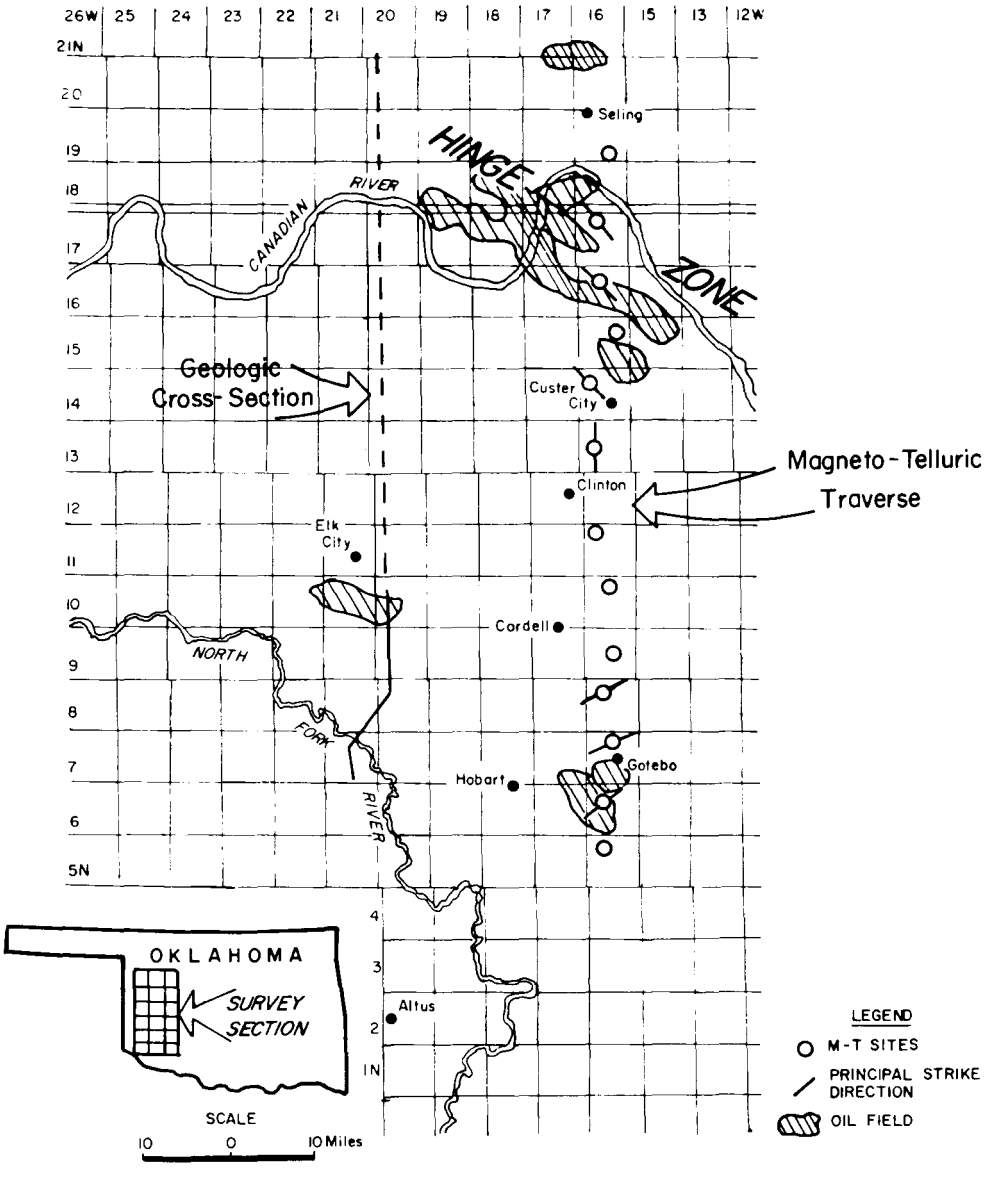

FIG. 33. Location map, Anadarko Basin traverse, Oklahoma, Ranges 20W–21W (after Lang, 1955 and Tulsa Geologic Society, 1951).

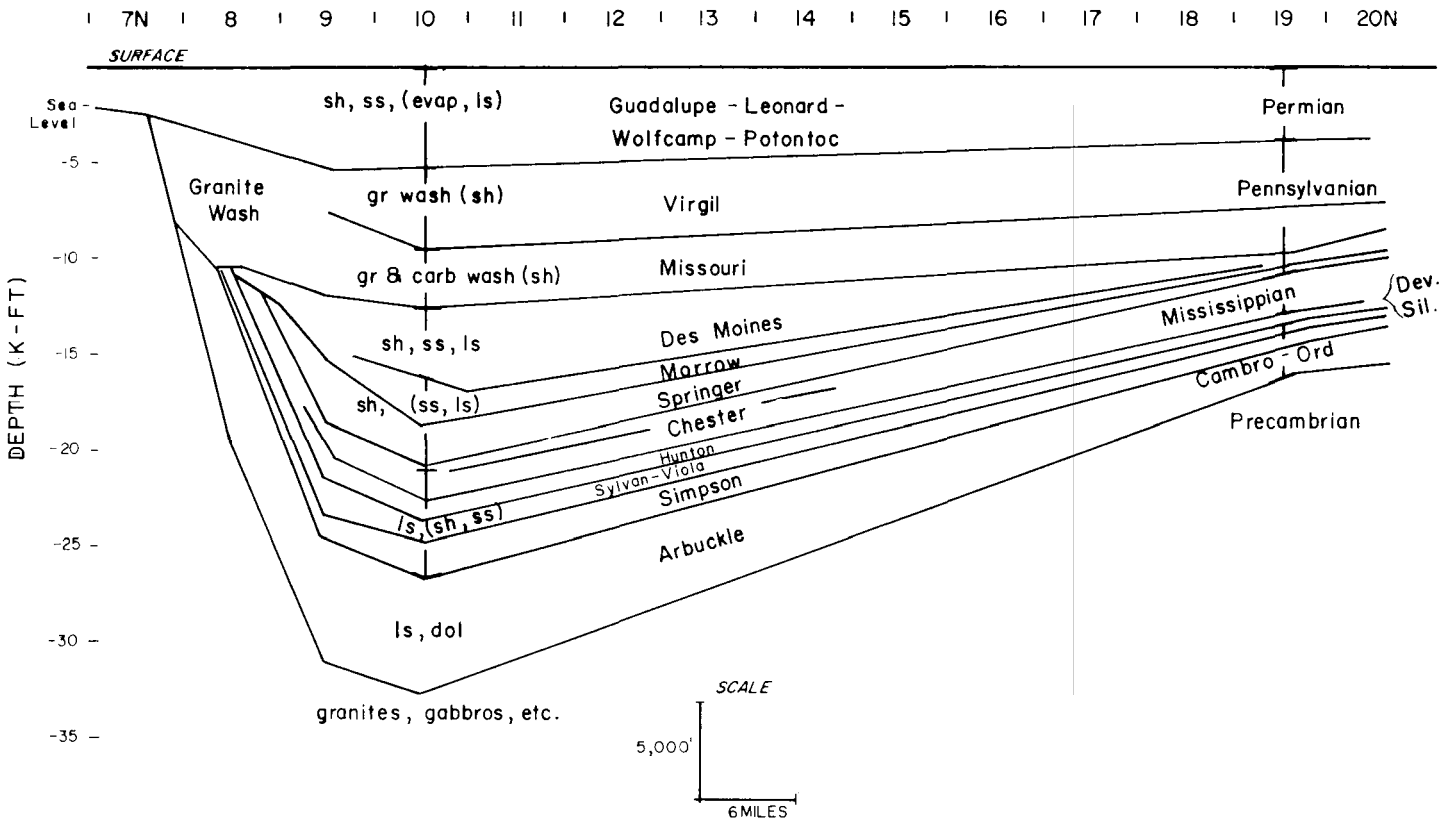

FIG. 34. Geologic cross-section 25 miles west of the Anadarko Basin traverse.

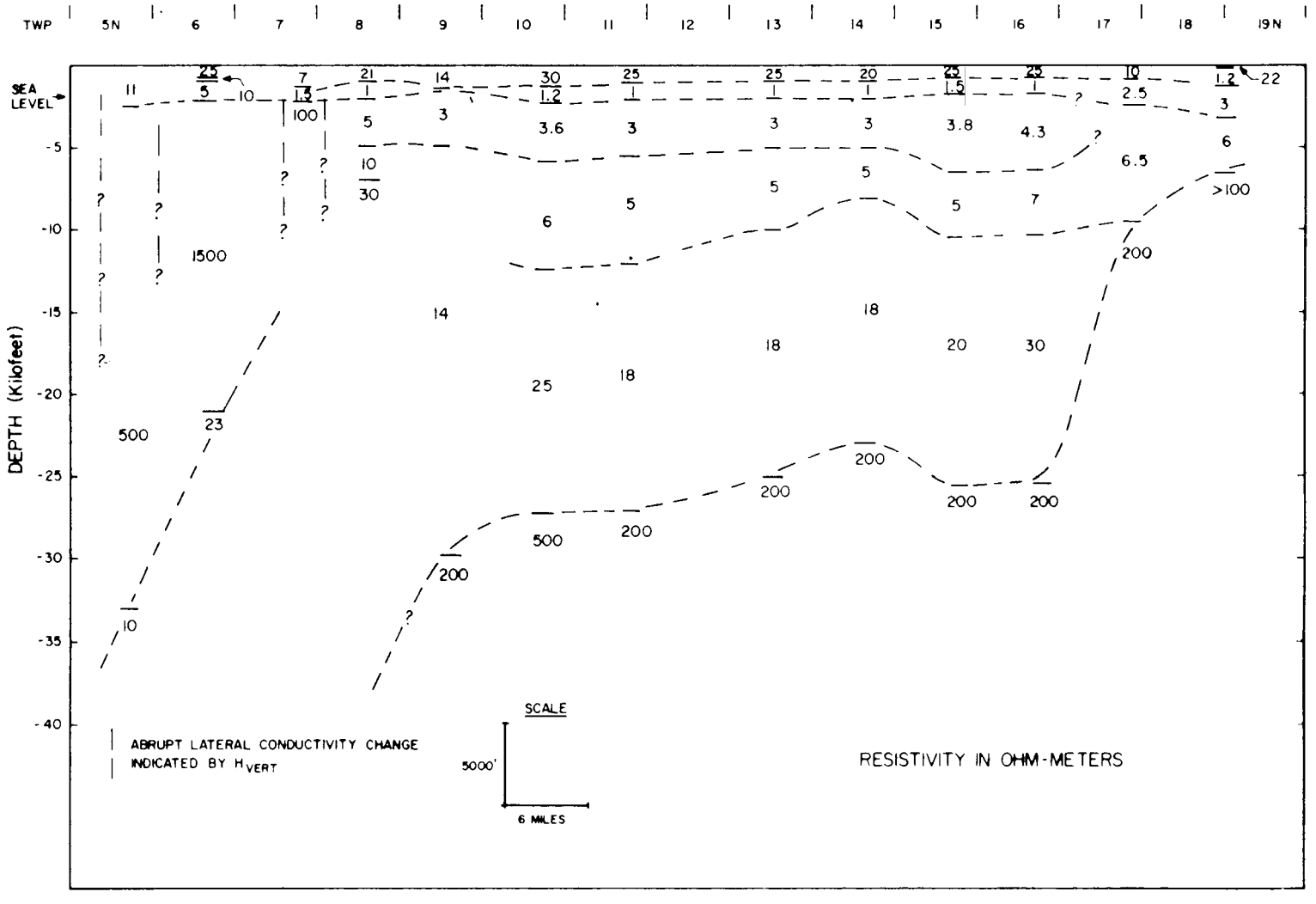

FIG. 35. Interpreted resistivity cross-section, Anadarko basin traverse.

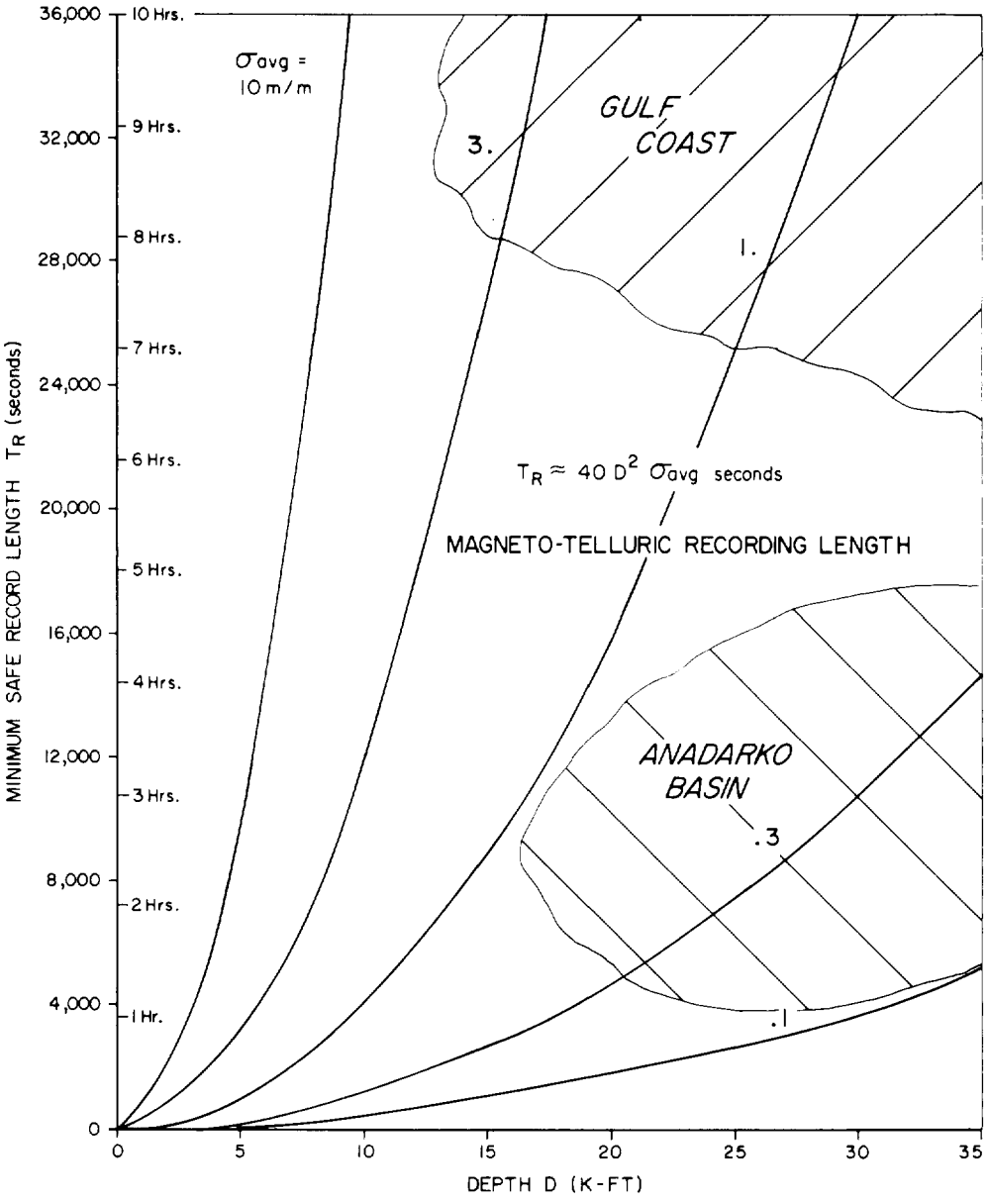

FIG. 36. Recording times under various conditions of section conductivity encountered in typical sedimentary basins.

basement rocks to a depth of approximately 8000 ft are layered Cambrian gabbros of the Raggedy Mountain group, a thick, layered intrusion made up of gabbros, anorthosite, and diorite. Where present, the Wichita granite group overlies the Raggedy Mountain gabbro as a thin veneer.

Moving from south to north, the first major structural feature encountered is the Meers Fault, where the basement drops abruptly from near-surface to a depth of approximately 10,000 ft. North of the Meers Fault is an area of complex faulting culminating in the Mountain View Fault, beyond which point the basement is at a depth of more than 35,000 ft. (The faults are not shown on this section.) Sediment thickness then re-

mains fairly constant for a distance of approximately 20 km when basement begins a shallow upward slope toward the Central Kansas uplift. North of the Meers Fault, the basement consists of layered rhyolite flows of the Carlton rhyolite group of Cambrian age. This has been inferred from drill holes penetrating through the Arbuckle group. The Carlton rhyolite group is thought to be underlain by a fairly thin granite zone and then bedded basaltic flows.

The sedimentary sequence is summarized on the cross-section. At the top are Permian red shales and sandstones with subsidiary evaporites and limestones. The major part of the section is Pennsylvanian, which may exceed 15,000 ft at its thickest. It includes substantial granite and carbonate washes, particularly at the south, underlain by shales with decreasing amounts of sands and limes. The underlying Mississippian consists primarily of limestones with subsidiary shale and sandstone beds, while the Cambro-Ordovician Sylvan, Viola, Simpson, and Arbuckle are primarily carbonates. The basal Reagan sandstone, not shown in the section, is very thin and intermittent, thickening to an estimated 100 ft in basement topographic lows.

Cutting diagonally across the traverse from NW to SE is a hinge zone, which crosses the traverse in the region of Twp 17 N. Facies changes in the Pennsylvanian are substantial and well-documented here, as well as farther south where the washes gradually terminate away from the mountains. The thick Arbuckle is also reported to contain major facies changes from limestone to dolomites, and from impermeable to very porous zones. From discussions with several geological specialists in this region, it appears to be generally believed that the faulting at the south end of the basin is of an overthrust nature, with the crystalline rocks overthrust to the north.

An intensive effort was made to estimate the resistivities of the rocks in the basin from subsurface logs, but this effort was unsuccessful because of the extremely conductive drilling mud used in the area. The values which were estimated apply only south from Twp 9 N. These are:

Virgil and Missouri Washes	10–25	ohm-m
Mississippian and lower Pennsylvanian	2–5	ohm-m
Arbuckle	50–250	ohm-m
Basement	100–5000 (locally 5 ohm-m).	ohm-m

The field program was, to the best of our knowledge, the first undertaken commercially in North America, fieldwork starting in early 1967. For purposes of objectivity, three geologists were involved independently in fitting layered models to the apparent resistivities. Each interpreted several nonadjacent sites, and the results were assembled and correlated by a fourth person, with the result shown in Figure 35.

North of Twp 7 N there was insufficient anisotropy to justify two-dimensional models. Such models were fitted to the more complex southern zone and resulted in some significant reinterpretation of the subsurface geological information there. For example, the trace of the large Mountain View Fault was shifted southward from its mapped location by over a mile.

The resistivity values correlate directly with rock type. Resistivities in the 100–200 ohm-m range correlate with low porosity carbonates and with some of the (probably factured) granites. Values greater than 1000 ohm-m seem to indicate more competent crystalline rocks. The 18–30 ohm-m resistivities at depth show the moderately porous limestone and sandstones, while the compactive effect of burial may drive the resistivities of limey and sandy shales into this range as well (McCrossan, 1961).

Considerable resemblance is evident between the electrical and geological cross-sections. Where they differ, the electrical section is in closer agreement with present geologic concepts of the basin. The Permian consists of three major subdivisions: a thousand feet or so of 10–30 ohm-m material at the surface, a similar thickness of 1 ohm-m material, and then 2000–3000 ft of 3–4 ohm-m rock. The Virgil and Missouri are made up of 6–30 ohm-m material in the granite wash facies and of a consistent 5–7 ohm-m material farther north. The remainder of the Pennsylvanian, the Mississippian, and portions of the Arbuckle comprise a massive thickness, with resistivities averaging about 20 ohm-m, within which little detail can be resolved. Beneath this mass, resistivity rises again by an order of magnitude. The low-resistivity values at depth at the south end strongly suggest that the resistive rocks forming the Wichita Mountains have been thrust over a large thickness of more conductive rocks. The resistivities of the latter are typical of the Lower Pennsylvanian and Mississippian rocks in the basin proper. The major lateral breaks of

the electrical cross-section bear a one-to-one correlation with the faults of Ham et al (1964). The abrupt resistivity change at depth in the hinge zone (Townships 16N–17N) may represent the effects of the extensive facies changes known to occur here (e.g., see Cambridge, 1970).

The smaller features are of questionable significance. For example, the apparent structure beneath Twp 14 at 25,000 ft can certainly be smoothed out with negligible effect on curve fit by minor changes in the shallower parameters. The structure at 10,000 ft could likely be reduced in size by similar reinterpretation, although it would require more effort to do so.

In this basin, the bulk resistivity is seen to increase with depth, from 1 ohm-m near the surface, to a few hundred ohm-meters in the basement. The apparent resistivity curves typically rise gradually with decreasing frequency over a very wide frequency range. Matching that portion of the curves requires only that resistivity increase at a well-defined average rate with depth. Neither the boundaries between layers nor the average resistivity within each layer can be very accurately determined in that depth range. A model made up of many thin layers, each more resistive than the one above, can be constructed that leads to practically the same result as the model consisting of a few thick layers.

The limits of interpretability of any set of data are shown clearly by two of the computer curve matching techniques now in use, the Monte Carlo searches (Greenfield, personal communication) and the generalized inversion technique (Harter and Madden, in preparation). Obviously, supplementary information regarding some parameters can be extremely useful in narrowing these limits for the remaining unknowns.

ECONOMICS

An MT operation involves field support, interpretive data processing, and logistical support. In a region of road access, a field crew would consist of 6–8 men, two of whom operate the equipment while the rest install and retrieve induction coils, porous pots, and wire. If surveying, linecutting, and station clearing are necessary, more men may be needed if no recording time is to be lost in waiting for site preparation. Data processing requires part or full time of one man, depending on the number of sites per day. Minimum recommended recording times per station for various regions are shown in Figure 36. Another major cost factor is the amount of geophysicist-geologist time spent on planning and interpretation. This can be limited in a routine investigation once it has been established that no unusual problems exist, but may require nearly full time for junior and senior interpreter in the interpretation stages of a nonroutine problem. Total costs in areas of road access have averaged about $2000 per site on a one site per day basis. Thus, the cost of the entire South Texas traverse was about $12,000, while that of the Anadarko Basin traverse was about $25,000.

Where logistics are more difficult, their costs can completely overwhelm those of the basic survey. Here the relatively small MT crew and the near-portability of the equipment lead to logistics costs which are much smaller than those of, say, a reflection seismic crew in the same area.

CONCLUSIONS

The results presented here clearly show the vast amount of significant geological information which the MT method can yield through careful application. Equipment and computer programs now available are functional, practicable, and generally reliable; but they could benefit from additional development. A higher speed (albeit cruder) reconnaissance capability, as practiced in the USSR (Yungul, 1971), leads to more favorable consideration of the method when rapid coverage at low cost is more important than great accuracy. Better display techniques would be of great help in comprehending and explaining the results.

Improvements continue to be made. For example, the accuracy and convenience of two-dimensional modeling can now be greatly enhanced by using the computer to space the networks which it then solves. Nevertheless, other approaches to modeling, such as those of Parry and Ward (1971) and Hohmann (1971), should be pursued, as should the development of analog models and analytical solutions for their obvious advantages. Research planned or in progress may in the next few years permit MT measurements to be made offshore and on unstable surfaces where they are not now possible.

With the range of questions that arise in the application of MT and the variety of tools which are available to the interpreter, each survey demands that decisions be made based on subjective,

preliminary evaluation. The correct decision is often critical to the technical and economic success of the survey. However, both our total understanding of the MT technique and our total knowledge of the gross electrical properties which it measures are still very limited. Hence, in order to obtain the best possible results from the method, planning and interpretation of surveys will probably have to continue to rely on specialists for some time to come. The alternative could be another 25 years of ignominy in petroleum geophysics for the electrical methods.

The magnetotelluric method has advanced tremendously in the past five years as a result of improved instrumentation, computer analysis, and (especially) interpretation. By and large, the method is well suited for mapping the broad features of porosity distribution and poorly suited for mapping fine detail. Its major potential contribution to oil and gas exploration appears to be in early stages of basin evaluation. An important secondary application is in exploration of areas which are unusually difficult to explore by conventional seismic means, such as areas of near-surface volcanic or metamorphic rocks or of very thick sands or gravels.

ACKNOWLEDGMENTS

The lessons and results reported here derive from the efforts of a highly professional team. Dr. G. H. Hopkins was responsible for the equipment; Dr. B. J. Woznick, for the data analysis programs; and Dr. J. N. Galbriath, Jr., for the data editing, data bookkeeping, and model-plotting routines. Messrs. A. Orange and H. S. Lahman ably supervised the field operations and data processing, and Mr. D. Halpin brought the essential outlook of the structural geologist to the interpretation group. Mr. R. Harter contributed significantly to development of the generalized inversion technique and also did much of its coding.

The novel analytical and interpretive tools which we used in this work were developed in the incisive researches of Prof. T. R. Madden and a group of outstanding students, notably, C. M. Swift, Jr., R. J. Greenfield, P. Nelson, and T. Cantwell, at MIT.

Drs. R. L. Caldwell and G. L. Hoehn suggested many improvements of presentation in early versions of this material. I am also indebted to the Rev. James Skehan, S.J., for his assistance, and to Dr. S. H. Yungul for a detailed reading and comments.

Funding for about half of this project was provided by a group of two major oil companies, while the remainder was sponsored by Geoscience, Inc., of Cambridge, Massachusetts.

REFERENCES

Cagniard, L., 1953, Basic theory of the magneto-telluric method of geophysical prospecting: Geophysics, v. 18, p. 605.

Cambridge, T. R., 1970, Potential of Marmaton oil production: Oil and Gas J., v. 68, p. 179.

Flawn, Peter, T., Chairman, 1967, Basement Map of North America: Basement Rock Project Committee, AAPG and USGS, Washington, D. C., Scale—1: 5,000,000.

Ham, W. E., Denison, R. E., and Merritt, C. A., 1964, Basement rocks and structural evolution, southern Oklahoma: Oklahoma Geol. Surv., Bull. 95.

Harthill, N., 1968, The CSM test area for electrical surveying methods: Geophysics, v. 33, p. 675.

Heirtzler, J. R., and Davidson, M. J., 1967, Synoptic measurements of geomagnetic field data: Tech. Report No. 1, CU-1-67 Nonr 4259(05), Lamont Geological Observatory (AD 665037).

Hohmann, G. W., 1971, Electromagnetic scattering by conductors in the earth near a line source of current: Geophysics, v. 36, p. 101.

Hopkins, G., 1965, Instrumentation for geofield measurements: EERL, Univ. Texas, Rep. No. 138.

Keller, G. V., 1968, Electrical prospecting for oil: Quart. Colo. School of Mines, v. 63, p. 38.

Kunetz, G., 1969, Traitement et interpretation des sondages magneto-telluriques: Rev. de l'IFP, v. 25, p. 685.

Lang, R. C., III, 1955, A geologic cross section from the Wichita Mountains to the Elk City pool: Shale Shaker Digest, p. 5.

Madden, T., and Nelson, P., 1964, A defense of Cagniard's magneto-telluric method: Geophysics Lab. MIT Project NR-371-401 rep.

Madden, T., and Swift, C. M. Jr., 1969, Magnetotelluric studies of the electrical conductivity structure of the crust and upper mantle: AGU Monograph 13, The Earth's Crust and Upper Mantle, p. 469.

McCrossan, R. G., 1961, Resistivity mapping and petrophysical study of Upper Devonian inter-reef calcareous shales of Central Alberta, Canada:Bull. AAPG, v. 45, p. 441.

Neves, A. S., 1957, The magneto-telluric method in two-dimensional structures: Dept. of Geology and Geophysics, MIT, Ph.D. thesis.

Nisenoff, M., 1969, Superconducting magnetometers with sensitivities approaching 10^{-10} gauss: Paper presented at C.N.E.S. Conference on Low Magnetic Fields, Paris.

Parry, J. R., and Ward, S. H., 1971, Electromagnetic scattering from cylinders of arbitrary cross-section in a conductive half-space: Geophysics, v. 36, p. 67.

Patrick, F. W., and Bostick, F. X., 1969, Magnetotelluric modeling techniques: EERL, Univ. Texas, Tech. Rep. No. 59.

Rikitake, T., 1966, Electromagnetism and the earth's interior: Amsterdam, Elsevier Publ. Co.

Sims, W. E., and Bostick, F. X., Jr., 1969, Methods of magnetotelluric analysis: EGRL Tech. Rep. No. 58, Univ. of Texas at Austin.

Smith, H. W., 1968, The magneto-telluric method—

field examples, Texas: Engineering Ext. Dept., Univ. Calif., Berkeley, Course notes.
Srivastava, S. P., 1967, Magnetotelluric two- and three-layer master curves: Dom. Obs. Publ., v. 35, no. 7, Canada Dept. of Energy, Ottawa.
Swanson, Donald C., 1967, Major factors controlling Anadarko Basin production: World Oil, p. 81.
Swift, C. M., Jr., 1967, A magnetotelluric investigation of an electrical conductivity anomaly in the southwestern United States: Ph.D. thesis, MIT.
Tikhonov, A. V., 1950, Determination of the electrical characteristics of the deep strata of the earth's crust: Dokl. Akad. Nauk, v. 73, p. 295.
Tulsa Geological Society (Hendricks, et al), 1951, Possible future petroleum provinces of North America, Mid-Continent region: AAPG, Tulsa.
Vozoff, K., and Ellis, R. M., 1966, Magnetotelluric measurements in southern Alberta: Geophysics, v. 31, p. 1153.
Vozoff, K., and Swift, C. M., Jr., 1968, Magneto-telluric measurements in the North German Basin: Geophys. Prosp., v. 16, p. 454.
Waeselynck, M., 1967, Etude de structures anticlinales ou synclinales par la methode magneto-tellurique: Bull. Centre Rech. Pau—S.N.P.A., v. 1, p. 417.
Wait, J. R., 1962, Theory of magneto-telluric fields: J. Res. N.B.S., v. 66D, p. 509.
Word, D. R., Smith, H. W., and Bostick, F. X., Jr., 1969, An investigation of the magnetotelluric tensor impedance method: EGRL Tech. Rep. No. 82, U. of Texas at Austin.
Wu, Francis T., 1968, The inverse problem of magneto-telluric sounding: Geophysics, v. 33, p. 972.
Yungul, S. H., 1961, Magnetotelluric sounding three-layer interpretation curves: Geophysics, v. 26, p. 465.
——— 1971, Personal communication.